DESIGN AND DEVELOPMENT OF AN ULTRASONIC POWER TRANSFER SYSTEM FOR ACTIVE IMPLANTED MEDICAL DEVICES

by

Peeter Hugo Vihvelin

Submitted in partial fulfilment of the requirements
for the degree of Master of Applied Science

at

Dalhousie University
Halifax, Nova Scotia
November 2015

TABLE OF CONTENTS

LIST OF TABLES

LIST OF FIGURES

ABSTRACT

Ultrasonic transcutaneous energy transfer (UTET) is a promising method for wireless power transfer to active implanted medical devices (AIMDs). Traditionally, AIMDs have relied on electromagnetic induction for wireless power transfer. However, when it comes to miniaturized power transfer devices, UTET has been shown to outperform EM based devices. In order to further the development of UTET devices for AIMDs, there are a number of design challenges which need to be addressed. This thesis work focuses on three key areas: i) the design and development of a feedback protocol for maintaining consistent UTET power transfer efficiency (PTE) across varying tissue separations, ii) the design and development of a high efficiency, high-frequency, low-power transmitter for driving the transmit side of a UTET link, and iii) the design and development of a high-efficiency rectifier and charging circuit for the receive side of a UTET link. The developed protocol for maintaining consistent PTE is shown to be extremely effective in regulating efficiency despite random changes in tissue separation; the protocol is tested in a realistic power transfer scenario through porcine tissue subject to random changes in inter-transducer separation distance. The designed transmitter is shown to operate with a peak efficiency of 93% at 1.28 MHz and an output power < 200mW. The designed receive circuitry is shown to have a full-wave rectification efficiency >90%; when paired with a high-efficiency DC-DC converter integrated circuit, the combined efficiency is ~70-80% for received powers > 40mW.

LIST OF ABBREVIATIONS AND SYMBOLS USED

ABBREVIATIONS

AC	Alternating current
AIMD	Active implanted medical device
DC	Direct current
eGaN	Enhancement mode gallium nitride
EM	Electromagnetic
EPC	Efficient power conversion
FOM	Figure of merit
MOSFET	Metal oxide semiconductor field effect transistor
MRI	Magnetic resonance imaging
PCB	Printed circuit board
PTE	Power transfer efficiency
PMN-PT	Lead magnesium niobate lead titanate
PZT	Lead zirconate titanate
RF	Radio frequency
Rx	Receive
Tx	Transmit
UTET	Ultrasonic transcutaneous energy transfer
Xdcr	Transducer

SYMBOLS

α	Attenuation
c	Sound speed
Δ	Difference in quantity
f	Frequency
f_p	Global optimum frequency

k	Magnetic coupling
k_t	Electromechanical coupling
λ	Wavelength
η	Efficiency
ρ	Density
P_{in}	Input Power
P_{out}	Output Power
Q	Quality factor
Q_m	Mechanical quality factor
T	Transmitted power ratio
Z	Acoustic impedance
Γ	Amplitude reflection coefficient
L	Channel length
GD	Gate drive
P_{GD}	Gate drive power
Vgs	Gate source voltage
f_{op}	Operating frequency
Q_g	Gate charge
P_{cond}	Conduction loss power
$R_{ds(On)}$	Drain source on resistance
R_{load}	Electrical load resistance
C_{oss}	Transistor output capacitance
I_d	Drain current
V_{ds}	Drain source voltage
I_{ds}	Drain source current
T_{on}	Rise time delay
T_{off}	Fall time delay
V_{cc}	Supply voltage
ω	Angular frequency
q	Reactance factor
Q_L	Loaded quality factor

ACKNOWLEDGEMENT

I would like to extend a sincere thank you to everyone who has supported me in different ways over the course of this Master's thesis. In particular, I would like to thank my supervisor, Dr. Rob Adamson, who has made the past few years extremely rewarding and has helped further my development as a biomedical engineer. He is a perfect example of what a graduate supervisor should be.

I am also thankful to Jeff Leadbetter, Chief Executive Officer at Daxsonics Ultrasound, for imparting his impressive knowledge of transducer design and construction on to me, and for fulfilling discussions on ultrasonics.

I would also like to extend my thanks and appreciation to my committee members who have provided valuable feedback to me throughout the course of my thesis: Dr. Jeremy Brown, Dr. Manohar Bance, and Dr. Zhizhang Chen.

Mom, Dad, Jess, and Alex: I can't thank all of you enough for the unwavering support you have provided. Adrienne: you've been with me through the thick and thin, and your words of encouragement have helped get me here.

This thesis is dedicated to my late grandparents, Lia Vihvelin & Dr. Hugo Vihvelin (Memme & Aia).

CHAPTER 1: INTRODUCTION

Active implanted medical devices (AIMDs), such as cardiac pacemakers and cochlear implants, have evolved significantly over the past decade. Research developments in the areas of battery technology, ultra-low power electronics, and new technologies for charging AIMDs from outside the human body have all come together to miniaturize AIMDs while also increasing their functionality and expected device life. When it comes to powering active implanted medical devices, some AIMDs are currently powered using implanted batteries which have limited stored energy and typically require periodic surgical replacement following the initial implantation. Other AIMDs, such as cochlear implants, make use of radio frequency (RF) electromagnetic fields for wireless power transfer from an external device to the implant; this form of wireless power transfer uses the principle of electromagnetic (EM) induction first discovered by Michael Faraday in the 1800s. While EM induction has seen widespread adoption for wireless power delivery to certain AIMDs, the overall wireless power transfer efficiency (PTE) for EM induction coils depends on coil geometry, the separation distance between coils, alignment, and other factors [1],[2]. Overall, the maximum possible PTE is limited by the magnetic coupling between coils, k, and the quality factor, Q, of each individual coil [3], [4]. The reported PTE values for EM induction coils scale with device size (i.e. larger coils perform better than smaller coils due to better magnetic coupling [3]). For implanted medical devices such as implanted hearing aids, the wireless PTE plays a large role in determining required battery-size and associated device run-time. A given external battery size, estimated average power requirement for the AIMD, and a desired device run-time, lead to a minimum link efficiency requirement.

In the implanted hearing aid industry, this translates to external and implanted coil sizes with diameters of ~ 20-30 mm, and typical battery-lifetime of 5-7 days depending on the device usage [5]. The relatively large size requirement for EM induction coils forces the use of bulky external and internal alignment magnets that help hold the coils in place. While the supporting electronics for implanted hearing aid applications are becoming more miniaturized, the required EM induction coil diameters have remained large which results in a bulky device that can only be implanted in certain locations. For reference, Figure 1 shows the implanted induction coil used for a cochlear implant along with a pediatric patient.

Figure 1: Implanted portion of a cochlear implant powered through magnetic induction (left) and photograph of a pediatric cochlear implant patient (right)

Ultrasonic transcutaneous energy transfer (UTET) is a promising alternative to EM coils for providing power to AIMDs, with the potential to greatly reduce the size of power transfer systems for AIMDS [6]. Smaller power transfer devices are beneficial to both surgeons and device users, as they allow more choice in implant location, shorter surgeries

and have more cosmetic appeal. Smaller power transfer devices also require smaller alignment magnets which can increase the MRI compatibility for the device [7].

UTET devices achieve electro-acoustic transduction through the use of piezoelectric materials. The term piezoelectric is used to describe the ability of certain materials to become electrically polarized when an external mechanical force is applied. Conversely, these materials show mechanical deflection in response to an electric field meaning that they compress or expand depending on the field's polarity. The piezoelectric effect has been used for many applications including force sensing, liquid flow sensing, and ultrasound medical imaging [3]. Two co-axially aligned piezoelectric transducers can be used to transfer energy through an acoustic channel, such as a water or tissue channel. By providing alternating electrical stimulation to one transducer, the piezoelectric effect causes the transmit piezoelectric material to expand and contract in a periodic manner. The mechanical action of the transducer creates an acoustic pressure wave that travels down the channel towards the receiving transducer. Once the pressure wave reaches the Rx transducer, it induces expansion and contraction of the piezoelectric receive transducer generating electrical energy that is transferred to a connected load.

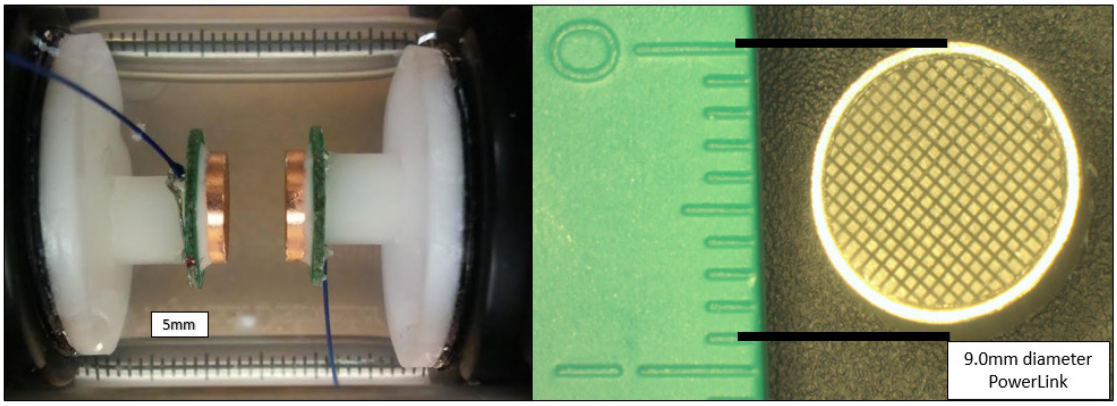

Figure 2: Constructed UTET link for powering AIMDs. Left-hand side shows power-transfer system transmitting power in a water-bath. Right-hand side shows a front face view of the composite transducer design.

A number of different research groups have published work on the design and development of ultrasonic links for powering implanted medical devices. However, the majority of the reported devices have diameters ≥ 15 mm which is large and does not represent much of an improvement in form factor over existing induction coils used for hearing implants. This led Leadbetter et al [8] to design and develop an ultrasonic link intended for implanted hearing aid applications. Their reported design used a matched pair of 5 mm diameter, 1.2 mm thick ultrasonic transducers capable of achieving a maximum PTE of 45 %. While the ultrasonic link itself represents a significant improvement over induction-based systems for implanted hearing aids, there are a number of engineering challenges that must be overcome in order to build a fully functional UTET device for powering hearing implants. The purpose of this thesis was to address three of these challenges related specifically to the design and implementation of drive electronics for a UTET link.

First, a number of different researchers [9],[10] have pointed out that the PTE of ultrasonic links shows a large dependence on the separation distance between ultrasonic transducers. A practical ultrasonic link must accommodate variable inter-transducer tissue separations from patient to patient, and be capable of operating with a predictable PTE in order to ensure implanted device functionality and a minimum run-time. While PTE variation is identified as an issue in the literature, and a potential direction for a solution to the problem is mentioned in [9] and [10], no researchers have described, designed, or validated a UTET system that can address this issue. Chapter 2 presents a detailed analysis of ultrasonic link PTE dependence on distance, a solution for eliminating this dependence, and test measurements that the solution works in a realistic scenario.

Second, piezoelectric transducers and their associated electronics have been well researched and developed for medical imaging purposes, however, there are relatively few published circuits for powering ultrasonic links. The most notable designs have been published by Ozeri et al [7]. In [7], transmit electronics that stimulate the transmitting transducer at 673 kHz are reported to operate with an efficiency > 90%. However, as ultrasonic links scale down in size, their required operating frequency must increases proportionally to avoid losses associated with diffraction and the design of high efficiency electronics is more challenging at high frequencies due to parasitic effects. For example, the ultrasonic links being developed in the Adamson group (and used in this thesis), operate in the frequency range of 1 to 1.5 MHz range. At these frequencies, based on simulations, the amplifier design proposed by Ozeri et al. would operate with < 85% efficiency. In order to develop high efficiency transmit electronics at higher frequencies, new approaches are necessary. Chapter 3 provides an analysis on power amplifier architecture for high-

frequency UTETs, and presents a high-efficiency Class E amplifier that achieves a peak efficiency of 93% at 1.28 MHz into a resistive load.

Third, on the receive side of an ultrasonic link, rectification electronics are required that are capable of taking the received alternating current (AC) stimulus and converting it into a usable direct current (DC) supply. In [7], Ozeri et al. were successful in the design of a high-efficiency rectifier network that operates with a reported efficiency of 89 % into a fixed resistive load. While the reported efficiency is high, the circuit is not representative of what would be needed for a practical AIMD which will present a time-varying electrical load. Further research efforts into rectification and energy storage for the implant circuitry are therefore needed before UTETs can be implemented in real devices. Chapter 4 presents the design and development of a high-efficiency rectifier and battery-charging circuit that is capable of powering a variety of implanted load demands.

The remainder of this chapter will review the literature on UTET links for active implanted medical devices. For the purposes of this review, only published results that include construction of a physical ultrasonic link are included. The research groups are presented in chronological order.

In 2001, Kawanabe et al [11], published their results using cylindrical lead zirconate titanate (PZT) transducers to transmit both power and data across the tissue of a living goat. The transducers operated at a frequency of 1 MHz, had a total thickness of 5 mm, and a 30 mm diameter. Their system obtained a PTE of 20% and a data-rate of 9.5 kbps using amplitude shift keying. The authors envision their system being used for multi-functional cardiac pacemakers which require relatively large amounts of power and a system for bi-

directional communication. In 2002, Suzuki et al [12] expanded on this research by implementing a two-path transmission system (employing two pairs of PZT transducers) in order to increase data-rates when communicating implanted device information to the exterior.

Five years later, Arra et al [13] presented their results using PZT transducers to transfer power and data through degassed water (degassed/deionized water is a standard test medium for ultrasonic transducers as it has similar acoustic properties to tissue, with the one exception being that water has negligible attenuation). The reported system used two transducers with mismatched 30 mm and a 25 mm diameter transducers (transmit and receive, respectively). The maximum PTE value achieved was 35% while average efficiencies ranging from 21-35% were measured from 5 mm – 105 mm of separation in deionized water.

In 2009, Ozeri et al [9] presented their research into using 15 mm diameter PZT transducers for power transfer. In their study, high efficiency transmit and receive electronic circuit designs were also presented (91.8% and 89% efficiency respectively [14]). A wireless PTE level of 27% (including rectification loss in the receive electronics) was achieved through 5mm of pig muscle. Ozeri et al [14] then furthered their researching into ultrasonic power delivery by designing a kerfless Gaussian-shaded transmitter which performed with an improved wireless PTE level of 39.1% through 5mm of pig muscle tissue. The increase in efficiency performance is attributed to a Gaussian-shaped diffraction field which has smaller pressure variations in the near-field and negligible pressure side-lobes.

In 2011, Shigeta et al [15] simulated and built a pair of PZT transducers designed to operate at 1.2 MHz. These transducers had matched diameters of 44 mm, thicknesses of 1.88 mm, and were shown to perform with a PTE of 50.4%; the separation distance for this test was not given. Also in 2011, Sanni et al. [16] demonstrated a two-tier interface which made use of both inductive and ultrasonic coupling. For the ultrasonic portion of the system, they used 10 mm diameter PZT transducers and report a PTE of ~ 1% across a 70mm tissue phantom (made of polysaccharide gel: 8.5% glycerol to water).

In 2013, Lee et al [6], reported their results using 50 mm diameter PZT transducers for ultrasonic power transfer. Their operating frequency was in the 200-300 kHz range, and the group achieved a maximum PTE of 55% in water and 21% through pig tissue. Also in 2013, Leadbetter, Brown, and Adamson [8] presented their results on using 5mm diameter composite lead magnesium niobate lead titanate (PMNPT) transducers. Compared to PZT, PMN-PT based transducers can be designed with a much higher electromechanical coupling coefficient, k_t. In the reported design, an electromechanical coupling of 0.77 is achieved through the use of a 'dice-and-fill' composite design. For this design, the transducer material gets subdivided into square pillars while gaps are filled with a soft fill material (EpoTek 301). The composite design allows the transducer's thickness mode oscillations to be more effective as the material's lateral stiffness is reduced. A maximum PTE of 45% was obtained in a water-bath using these devices.

The results from this literature review are summarized in Table 1.

Research Group	Material	Diam. (mm)	Thick. (mm)	Freq. (MHz)	Max η (H2O)	Max η (Tissue)
Kawanabe et al. [11]	PZT	30	5	1	---	20%[2]
Suzuki et al. [12]	PZT	30	2.0	1.0	20%	---
Arra et al. [13]	PZT	30, 25	---	0.840	35 %[2]	---
Ozeri et al. [9]	PZT	15	3	0.673	38 %[1]	27 %[1]
Ozeri et al. [14]	PZT	15	3	0.673	---	39.1 %[2]
Shigeta et al. [15]	PZT	44	1.88	1.2	50%[1]	---
Sanni et al. [16]	PZT	10	---	0.2	---	~ 1 %[1, 3]
Lee et al. [10]	PZT	50	---	0.2-0.3	55%[2]	21%[2]
Leadbetter et al. [8]	PMNPT	5	1.2	1.07	45 %[1]	---

Table 1: Summary of research groups that have reported ultrasonic links intended to provide power to AIMDs. [1]Transducer link efficiency, [2]End-to-End electrical efficiency, [3]Test performed across ~70mm of tissue phantom, [4]2.5cm separation.

The remainder of this thesis will cover the following:

Chapter 2 will present one of the key challenges in designing a practical ultrasonic link, discuss the potential solutions to this design problem, present a proposed feedback protocol for maintaining high PTE in the presence of acoustic channel variations and cover its performance in a realistic power transfer scenario. Chapter 3 will present the design requirements for a high efficiency amplifier circuit suitable for driving the transmit side of an ultrasonic link, discuss various amplifier design topologies and their suitability, show the design process for the chosen amplifier topology, and outline both its simulated and experimental performance. Chapter 4 will present the design requirements for a high efficiency receive circuit for capturing energy from the receive side of an ultrasonic link, discuss various rectifier design topologies and their suitability, cover the chosen design and

its circuit components, and then outline both its simulated and experimental performance. Finally, Chapter 5 will outline the main contributions of this thesis to UTET power delivery technologies for AIMDs and present suggested areas for future research efforts.

CHAPTER 2: MAINTAINING MAXIMUM POWER TRANSFER EFFICIENCY LEVELS IN AN ULTRASONIC POWER LINK FOR BIOMEDICAL IMPLANTS

A typical ultrasonic power link system for medical implants, depicted below in Figure 3, consists of a piezoelectric transducer and its associated drive electronics, a volume of tissue that ultrasonic energy propagates through, and an implanted piezoelectric transducer along with its associated receive electronics which provide power to the implanted device. In the figure, the energy drawn by the medical implant is depicted by a resistive electrical load, *Rload,* while the acoustic wave travelling through the tissue is shown to span 2.5 wavelengths.

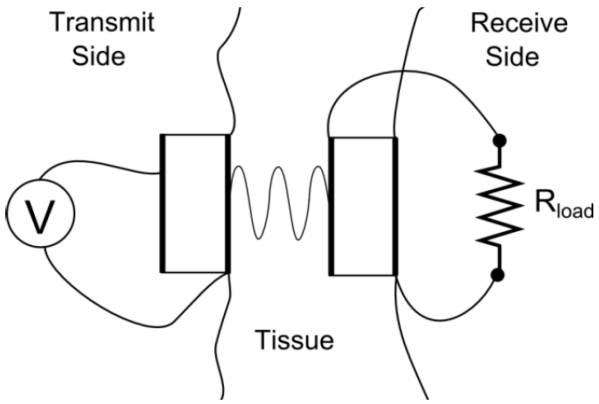

Figure 3: Schematic illustration of an ultrasonic power transfer system for medical implants.

Ultrasonic power link systems can be characterized by their power transfer efficiency (PTE) which is defined as the ratio between their electrical output power and input power ($\eta = P_{out}/P_{in}$). An ultrasonic link's PTE can show extreme sensitivity to the

transmitting frequency and/or the separation distance between the transmit and receive transducers [1], [2]. In a coupled implanted ultrasonic power link the separation distance will be dynamic, potentially changing with time, a patient's hydration level, implant location, and other factors and varying from patient to patient. Without understanding and compensating for the effect of separation on power transfer efficiency, ultrasonic link technology would remain highly impractical. In this chapter, the effects of separation distance on an ultrasonic link were studied in order to develop a protocol for maintaining maximum power transfer efficiency regardless of separation distance.

A paper on this topic was published in IEEE Transactions on Biomedical Circuits and System, for full reference please refer to the list of contributions.

If the power transfer efficiency for two similar but slightly different water separations is measured, the two PTE spectra look very similar, but are frequency-shifted copies of one another with the amount of shift depending on the separation. Below are the measured PTE spectra for two co-axially aligned 8.00 ± 0.005 mm diameter PMN-PT transducers in a water-bath. For the blue curve the water separation distance was 5.88 ± 0.07 mm and for the green curve the separation was 6.11 ± 0.07 mm. In the figure, it is clear that the frequency of maximum efficiency for the two channel lengths is different while the maximum attainable efficiency value remains similar.

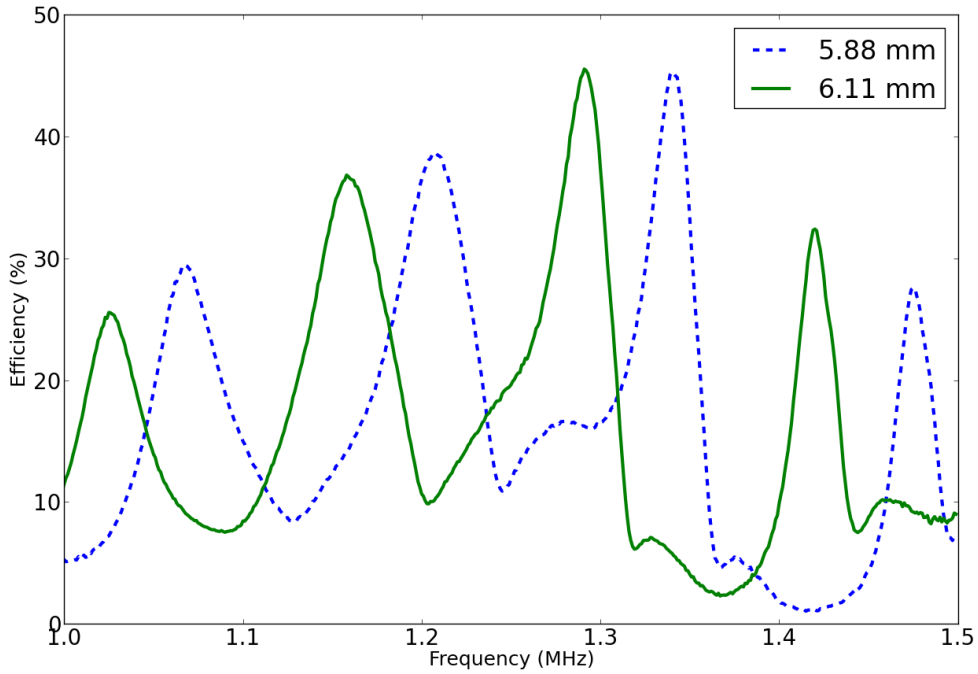

Figure 4: PTE spectra for a coupled ultrasonic link at two different water separation distances. The ideal operating frequency for the 5.88 mm case is 1.34 MHz while that for the 6.11 mm case is 1.29 MHz

Ultrasonic PowerLink System Description

In order to better visualize a coupled ultrasonic power link system, we can refer to the diagram in Figure 5 where there are two co-axially aligned piezoelectric elements, separated by a 6.0 mm water transmission channel. Attached to the front and rear electrode of the transmit transducer (Tx Xdcr) are transmitting electronics which apply an alternating current (AC) stimulus in order to vibrate the piezoelectric element at a particular operating frequency. Vibration of the piezoelectric element creates a pressure wave in the water. On the right-hand side of Figure 4, a receive transducer (Rx Xdcr) is used to re-convert energy

from the incident pressure wave back into its electrical form through the direct piezoelectric effect.

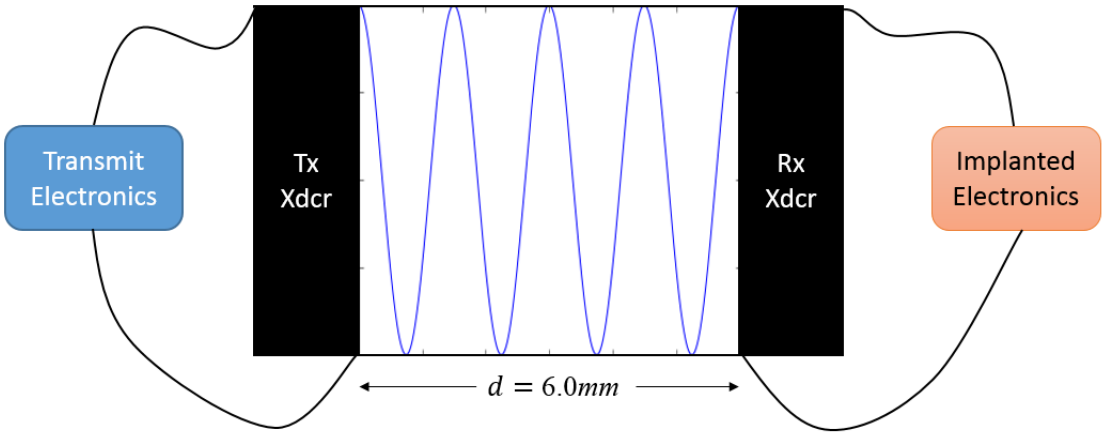

Figure 5: Depiction of two co-axially aligned transducers transmitting through a 6.0mm water transmission medium. The pressure wave depicted is travelling at 1496 m/s in the water medium and the operating frequency of the transducers is 1.0 MHz giving a wavelength of 1.5 mm and 4 wavelengths in the cavity [3].

Finite element models and measured results of the pressure field developed between two co-axially aligned transducers reveal that standing waves and travelling waves develop between the transducers during power transmission [9], [4]. The water channel or tissue medium separating the two transducers forms an acoustic cavity which has its own resonances associated with it. The behavior for the coupled acoustic system (consisting of the transmit transducer, water/tissue medium, and receive transducer) is highly dependent on the acoustic impedance and attenuation of the water/tissue medium. Within the channel the acoustic wavelength, λ is defined by Equation (1) where c represents the sound-speed in the transmission medium and f represents the operating frequency.

$$\lambda = \frac{c}{f} \qquad (1)$$

For a given acoustic layer, attenuation (denoted by α) accounts for losses due to scattering and absorption while acoustic impedance, Z, defines the reflectivity that will be experienced by waves travelling from that layer to another layer. The characteristic acoustic impedance, Z, for a given material depends on its longitudinal sound-speed, c, and its density, ρ, according to Equation (2).

$$Z = \rho c \qquad (2)$$

For a wave that is travelling from one acoustic layer to another, the amplitude reflection coefficient, Γ , is dependent on each layer's acoustic impedance and is given by Equation (3). Z_2 is the acoustic impedance of the second medium and Z_1 is the acoustic impedance for the first medium.

$$\Gamma = \frac{Z_2 - Z_1}{Z_2 + Z_1} \qquad (3)$$

The ratio of acoustic power that gets reflected at a boundary is defined by $|\Gamma|^2$ given in Equation (4) while the remaining power gets transmitted through the boundary according to Equation (5).

$$|\Gamma|^2 = \left|\frac{Z_2 - Z_1}{Z_2 + Z_1}\right|^2 \qquad (4)$$

$$T = 1 - |\Gamma|^2 \qquad (5)$$

If we reconsider the system given in Figure 5 in terms of its acoustic components, the following block diagram in Figure 6 can be used to help understand and visualize wave behavior in the system.

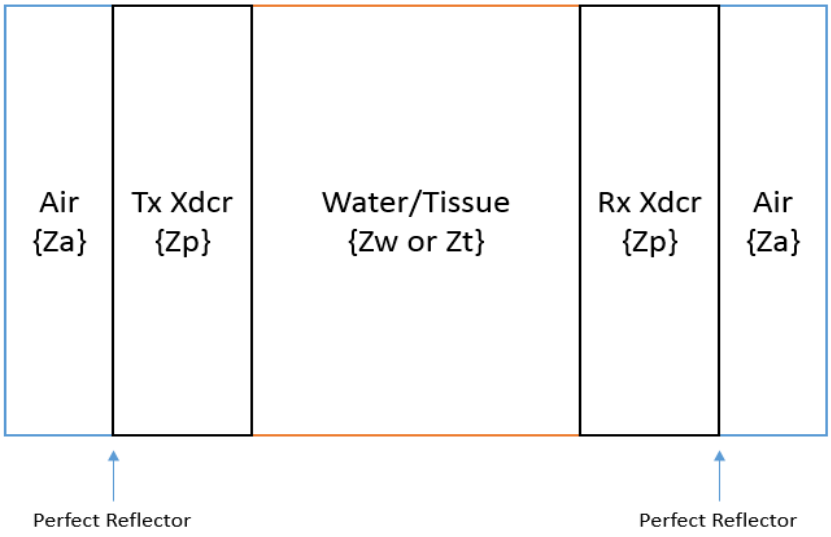

Figure 6: Acoustic components for the coupled ultrasonic power link. In brackets, the subscripts for each layer's acoustic impedance is given. Each transducer has an air-backing in order to maximize energy transfer.

In order to maximize energy transfer both the transmit and receive transducers make use of an air-backing in power transfer applications. The impedance of air is 429 Rayls ($N \cdot s/m^3$) while the impedance of PMN-PT is 33.6 MegaRayls which results in a reflection coefficient of > 0.99 meaning near-perfect reflection occurs at the air-piezoelectric interface due to the impedance mismatch [5], [6]. This effect is desired for power transfer applications in order to maximize the transmitted or received energy.

Considering the coupling medium between the two transducers, the average acoustic impedance for soft tissue is 1.63 MegaRayls with water having a similar acoustic impedance (1.48 MegaRayls) [17]. For reference, Table 2 provides the acoustic impedance and attenuation for water and different tissues in the human body.

Material	Acoustic Impedance (MegaRayls)	Attenuation (dB/cm
Connective tissue	1.81	1.57
Fat	1.40	0.48
Muscle	1.62	1.09
Tendon	1.84	4.7
Soft tissue	1.63	0.54
Water	1.48	0.0022

Table 2 :Acoustic impedance and attenuation properties for various tissues [17]

Without the use of intermediate acoustic matching layers (which facilitate acoustic wave propagation from one layer to another) the acoustic impedances of PMN-PT and soft-tissue result in a reflection coefficient of 0.9075. This acoustic impedance mismatch results in a highly reverberant and frequency-selective system [18] as evidenced by the initial power transfer efficiency spectra shown in Figure 4. Acoustic waves within the system must travel through a number of different acoustic paths before being converted into electrical energy. The maximum possible PTE for an ultrasonic link depends on the characteristic impedances that are present in the system and the losses present within each element or layer. Piezoelectric elements can be characterized by their mechanical quality factor, Qm, and their mechanical loss is proportional 1/Qm. For acoustic waves travelling within the acoustic cavity, attenuation and wave interference also become important. Attenuation is a fixed material loss and cannot be compensated for. However, as mentioned above, the acoustic cavity formed by the water channel or tissue medium has its own resonances associated with it. These resonances appear in the electrical impedance of the transmitting element, and turn out to be crucial in determining the correct operating frequency for maximum power transfer efficiency.

Transducer Electrical Impedance

Piezoelectric elements are electromechanical devices and couple electrical energy into mechanical motion, which means their electrical impedance is affected by the mechanical load they are connected to. Below is the measured electrical impedance (in magnitude and phase) for an 8.00 ± 0.005 mm diameter composite PMN-PT transducer in air. In Figure 7 the impedance magnitude minimum occurs at 1.015 MHz and the impedance magnitude maximum occurs at 1.596 MHz. The latter frequency can be designed for by setting the thickness to make the device a half-wave resonator. The impedance curve for a given transducer can also be used to estimate various transducer properties such as the electromechanical coupling coefficient, k_t. The wavelength within the transducer is set by Equation (1) where c represents the sound-speed in the material and f represents the desired operating frequency. By making the piezoelectric thickness equal to $\lambda/2$, a half-wave resonator is created. Waves travelling in the device at the operating frequency reinforce themselves as the round-trip wave phase is equal to the initial wave's phase. Importantly, in Figure 7 there is only one resonance within the measured impedance spectrum meaning the dominant mode for this transducer is in the thickness direction. This is a desired trait as other modes of vibration can couple to the transverse mode resulting in non-radiative loss mechanisms for acoustic power.

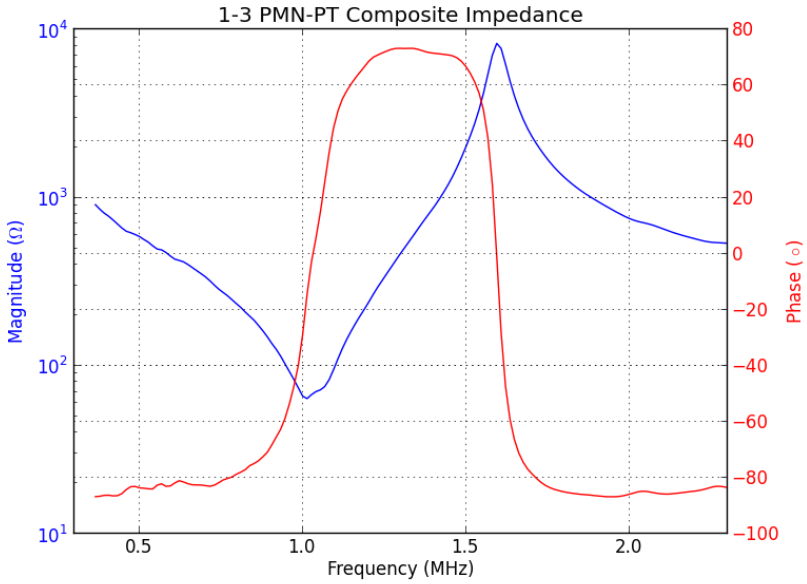

Figure 7: Electrical impedance in magnitude and phase for an 8.00 mm diameter composite PMN-PT transducer in air

When the transducers are water-coupled, the measured impedance spectrum is affected by water loading on the transmitting device and the presence of the piezoelectric receiver which can receive energy and reflect energy back toward the transmitter. Below is the measured electrical impedance for a transmitter coupled through 6.0 mm of water to a receiver. In the figure, there exist many narrow resonance/anti resonance pairs that correspond with cavity modes of the water channel. The broad features correspond to the uncoupled piezoelectric impedance shown in Figure 7.

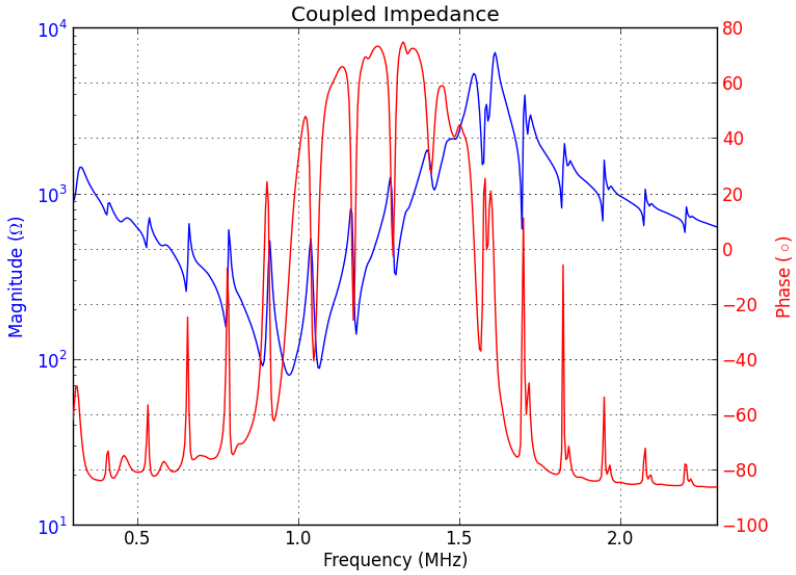

Figure 8: Coupled electrical impedance (magnitude and phase) for a transmitting piezoelectric coupled through 6mm of water to a receiving element

The frequency separation between impedance features for the water channel are defined by a frequency, Δf, which corresponds to the round-trip resonant condition for waves travelling in the channel. Δf can be calculated from (6).

$$\Delta f = \frac{c}{2L} \qquad (6)$$

If we consider a 1.0 MHz acoustic wave in water, it has a wavelength of 1.5 mm using Equation (1) with a sound-speed of 1499 m/s. For this static frequency, only water channels that are an integer multiple of 0.75 mm satisfy the condition for resonance. The

overall effect that this resonance condition for the transmission channel has on power transfer efficiency can depend on the particular transducer design and channel properties such as length and attenuation. In our designed system, we are using air-backed 1-3 PMN-PT composite transducers to transmit power through approximately 5 to 7 mm of tissue. Experimental results for this type of scenario reveal that power transfer efficiency levels can vary by over 40% as the channel distance is varied over half a wavelength. Since acoustic distance will change with patient movement, hydration, and tissue growth, a technique for reducing this effect is required to make UTET links practical.

Developing a Compensation Strategy for Maximizing Power Transfer Efficiency

In the previous section, it was shown that the power transfer efficiency spectrum for a coupled UTET link depends strongly on channel separation distance. While channel separation distance cannot be easily controlled in a biomedical UTET system, Figure 4 shows that maximum power transfer efficiency can obtained by adjusting the drive frequency to compensate for tissue length changes. In this section, we will propose a feedback protocol for measuring changes to acoustic channel length and modifying drive frequency in order to maintain maximal efficiency.

There are a number of different approaches that exist to potentially compensate for changes in channel separation distance. One approach would be to make use of a separate communication link. Periodic frequency sweeps paired with measurements of input power and received power would yield the efficiency versus frequency spectrum directly. However, not all implanted medical devices that could benefit from this kind of a

transcutaneous energy source have a readily-available two-way communication link. For these types of devices, the additional implanted electronics and communication link represent a cumbersome addition to the design.

A more universal approach to keeping track of the ideal frequency of operation in a UTET link is available due to the electromechanical nature of the transmitting piezoelectric. Below is a simultaneous measurement of power transfer efficiency along with the measured transmitter electrical impedance in magnitude and phase, for two separation distances. The blue curve represents a water separation of 5.88 mm and the green curve represents a water separation of 6.11 mm.

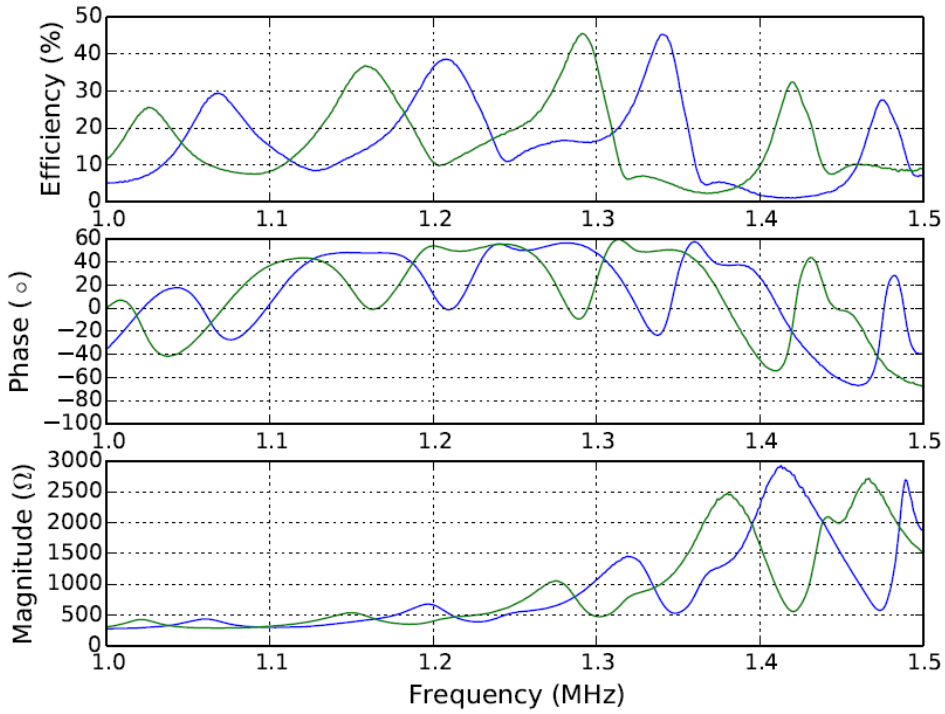

Figure 9: Power transfer efficiency, and electrical impedance (magnitude and phase) for a coupled ultrasonic link transmitting through 5.88 mm and 6.11 mm of water (blue and green curves respectively)

Importantly, the channel resonances can be identified within the impedance magnitude and phase as significant deviations from the uncoupled piezoelectric impedance curve. From the figure, it is also apparent that the local minima in transducer impedance phase tend to correspond well with the local maxima in efficiency between 1.1 and 1.4 MHz. Between 1.0 and 1.1 MHz, and 1.4 and 1.5 MHz, the impedance phase minima show less agreement with the local efficiency maxima due to the fact that the piezoelectric impedance phase in these areas is also changing. Figure 9 also shows that the power transfer efficiency values obtained at each channel resonance (for a single separation distance) also vary. It is therefore insufficient to locate a single channel resonance and then operate at that frequency. This feature for the PTE spectra suggests that the ultrasonic power link has its own global optimum frequency.

Determining the Ultrasonic Power Link's Global Optimum Frequency, f_p

Equation (6) predicts that as channel separation between a coupled transducer pair is increased, the resonances tend to shift to lower frequencies and the separation between resonances becomes smaller. However, while the frequency for local efficiency maxima correspond directly with separation distance, the global maximum efficiency occurs at a frequency determined by both the separation distance and the piezoelectric transducer response. In order to find the global best operating frequency for a transducer pair, the locations of each local maximum in efficiency were plotted over a range of separation distances that spanned multiple wavelengths. Figure 10 is a scatterplot that shows this measurement for water separations that span approximately 3.0 to 7.0 mm.

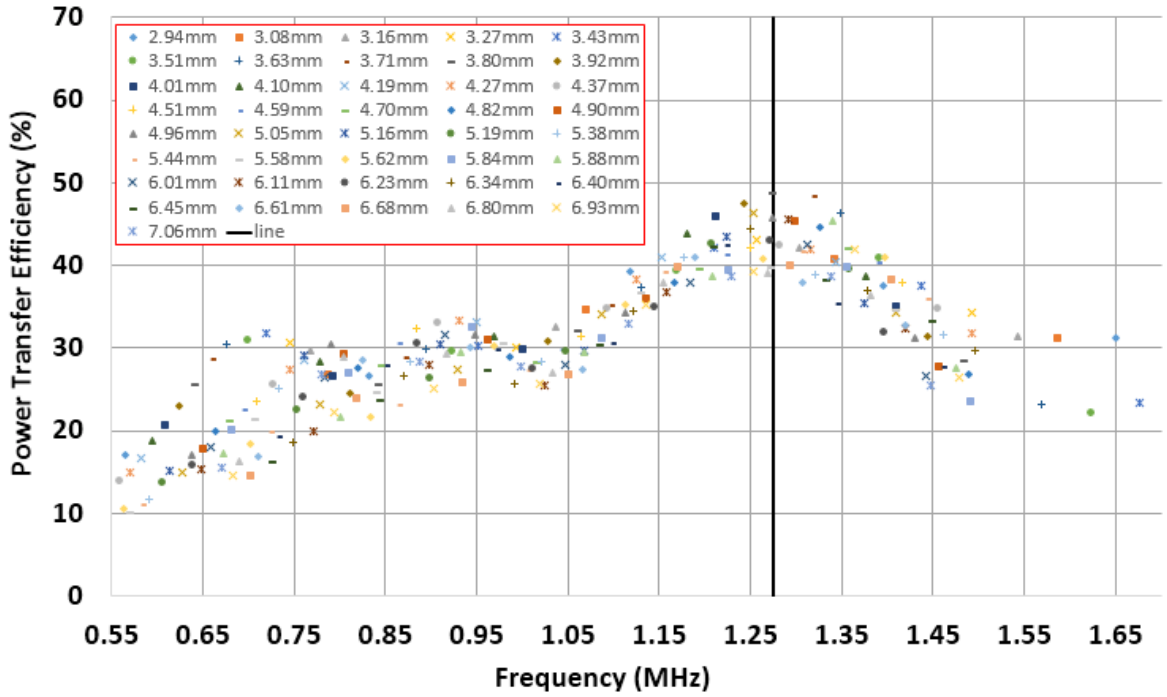

Figure 10: Scatter plot of local maxima in power link power transfer efficiency over a range of separation distances that span 3mm to 7mm. The vertical line shows the global efficiency maximum.

In the ideal power transmission scenario for this coupled set of transducers, a channel resonance condition would coincide with the global optimum for the transducers (located at 1.275 MHz). However, Figure 6 shows that high transfer efficiencies can be obtained over a wide range of separations if frequency tuning is implemented since for all separations there are frequencies for which the efficiency exceeds 37% compared to a maximum of 45%.

The global optimum represents the frequency at which the piezoelectric transducer and electronics optimally convert electrical drive power into acoustic power. The global optimum, defined in this way, is independent of channel length and thus, it is reasonable to expect deviation from the global optimum frequency to result in reduced power transfer

efficiency values. In the following section, the global optimum frequency for the ultrasonic power link is determined. For the rest of this chapter, we will denote this global optimum value by f_p.

Within Figure 9 there is still some variation in the maximum achievable efficiency which can be attributed to the 2 dimensional nature of the system. As the transducers are moved further apart, the transmit and receive transducer alignment varies and diffractive effects will cause efficiency variation. In a practical implementation for the power link, it is important to know the overall required tuning range such that power transfer efficiency can always be maximized.

Determining the Power Link's Required Frequency Tuning Range

In order to characterize the frequency tuning required for a subdermally implanted ultrasonic power link, the measured channel resonant frequency closest to f_p can be plotted against the expected range of separation distances. For this analysis, the frequency-swept data acquired in the previous section was re-analyzed as 3.0 to 7.0 mm of tissue separation is the design range for an ultrasonic power link located at a patient's mastoid tip [7]. Over the range of these separations, the measured channel resonant frequency closest to f_p was recorded. Figure 11 shows the measurement result.

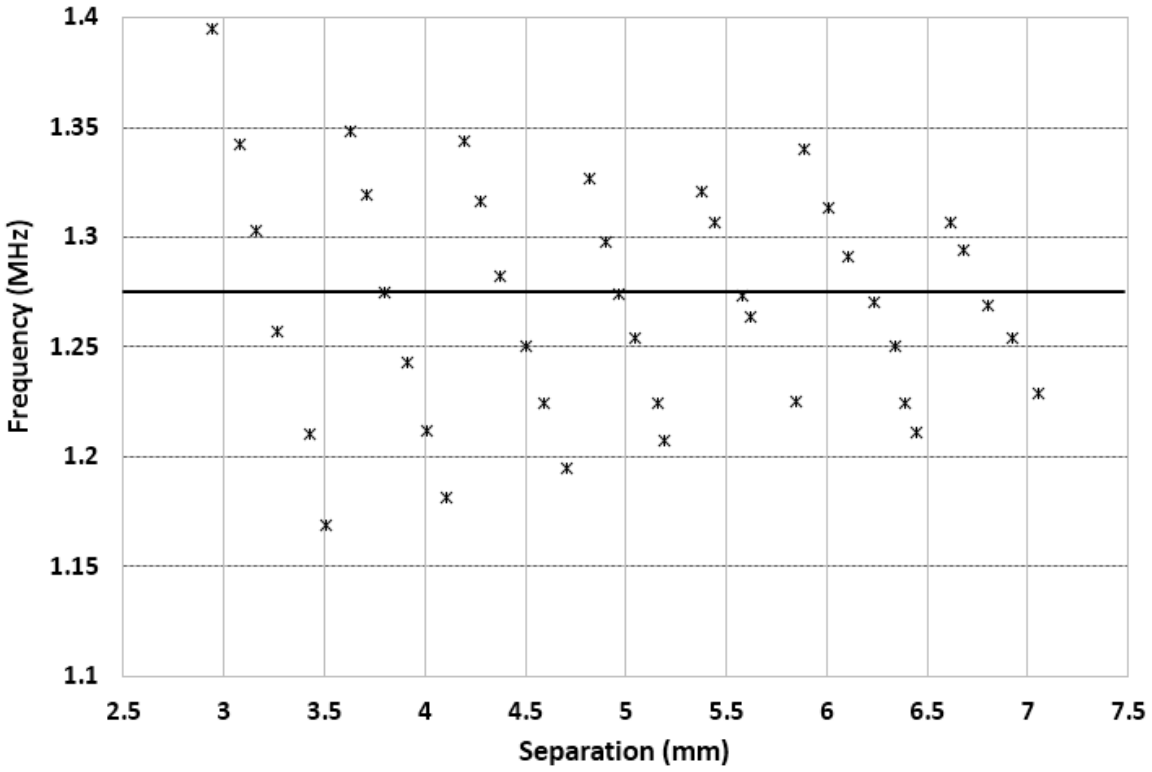

Figure 11: Channel resonant frequency closest to the transducer pair's global optimum frequency (denoted by the black horizontal line at 1.275 MHz) over varying separation distances

As the transducers are moved further apart, there are two different effects. The required frequency tuning range narrows which corresponds well to the theory for a resonant cavity and its associated value for Δf defined by Equation (6). As the separation distance increases, Δf decreases bringing channel resonances closer together which is also consistent with Equation (6). For reference, Figure 12 gives the channel resonant frequencies for channel lengths spanning 3.0 to 7.0 mm in increments of 0.25 mm. These channels have Δf values in the range of 107-214 kHz and are multiplied by the integer values {5,6,7,…14} in order to show resonant frequencies between 1 and 2 MHz.

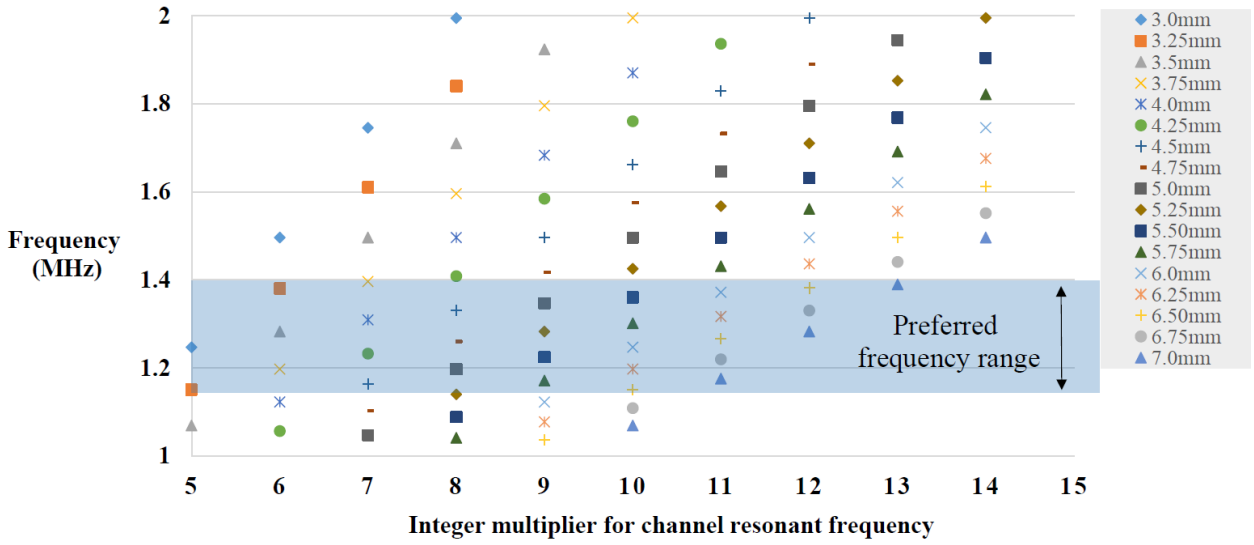

Figure 12: Depiction of channel resonant frequencies for varying separation distances. The value for the initial resonance is calculated using Equation (6) with a sound speed of 1496 m/s. The individual channel lengths are noted in the legend. The preferred frequency range depicts frequencies for which the efficiency remains >34%.

It is clear from the figure that larger channels can bring additional resonances into the preferred tuning range for the ultrasonic power link (highlighted and shown with an arrow in Figure 12). Additionally, the vertical frequency spacing between resonant points for increasing channel lengths decreases linearly. These two features are reflected in the required tuning range shown to decrease linearly with distance in Figure 11.

As the separation distance is increased, the transmit frequency of operation needs to be tuned lower in order to operate at the point of maximum power transfer efficiency. Conversely, if the separation distance is decreased it needs to move higher up to a point and then there is a discontinuity. If we consider an acoustic wave within a cavity, the effect that separation distance has on the frequency for maximum efficiency can be understood.

For channels that are resonant with the acoustic wave (i.e. integer multiples of its half-wavelength value), then a resonance condition has been met. If the channel is shortened by a small amount (much less than a quarter wavelength) then the channel's resonant frequency modes change according to Equation (6). Resonance can then be regained by a small increase in the acoustic wave's frequency, or a much larger decrease in the frequency. Either increasing or decreasing the frequency has the potential to put the channel back into resonance. However, when piezoelectric transducers are used to excite acoustic waves the power transfer efficiency will also depend on the detuning from the transducer pair's global optimum, f_p, denoted by the solid line in Figure 11. Over the measurement range, the frequencies of maximum efficiency are symmetric about f_p. However, there are points in Figure 11 where there exists a discontinuity in the curve. As separation increases and the channel resonant frequency moves to lower frequencies, eventually there is a separation distance where either increasing or decreasing frequency could lead to the optimal efficiency value (for example between 3.5 and 3.6 mm in Figure 11). These points occur when the cavity is a quarter wavelength from resonance so that the frequency tuning required to regain resonance is the same whether the frequency is increased or decreased. In these cases, the efficiencies attained by increasing and decreasing the frequency are equal to within experimental error.

Overall, patient movement, hydration, tissue growth, and weight changes [7] are all expected to cause changes in the acoustic separation which can cause efficiency reductions in a fixed frequency ultrasound power transfer system. However, based on the discussion above, a system capable of dynamic frequency compensation can maintain maximum

power transfer efficiency if it is also capable of determining (and operating at) the channel resonance closest to the transducer pair's global optimum, f_p.

Using Impedance Phase to Track Frequency of Maximum Efficiency

If a designer knows the transducer pair's global optimum frequency, f_p, along with an estimate of the frequency tuning range required for the expected channel lengths to be encountered, it is relatively straightforward to develop a feedback protocol for tracking the nearest channel resonance (maximizing power transfer efficiency) based on the transmit transducer's electrical impedance phase. An initial measurement of the impedance phase spectrum is required in order to determine the locations of individual channel resonances. For the particular transducers involved in this system and the known required tuning range, the minima in impedance phase can be used to adequately pick out the resonances as the impedance phase is relatively flat over the required tuning range. Once the channel resonances are determined the system only needs to pick out the closest resonant point to f_p as the operating frequency. A controlled experiment was designed in order to assess the performance of this frequency tuning algorithm based on impedance phase measurements.

Real Time Frequency Compensation Experiment Using Porcine Tissue

The experiment was conducted using the ultrasonic power link and a 5mm ± 0.5mm porcine tissue sample composed of approximately 2 mm of epidermis and dermis, and 3 to 4 mm of subdermal fat. This porcine tissue is an approximate model for the issue that is expected for a cochlear implant powering device. An Agilent 33210A function generator was used to drive the transmit transducer while an Agilent DSO6014A oscilloscope was used to monitor the transmit voltage, transmit current, and receive voltage, allowing for

calculation of input power, output power, and complex impedance for the transmitting transducer. Custom Python scripts running on a PC were used in order to automate and run the experiment. A block diagram of the experimental setup is shown below in Figure 13.

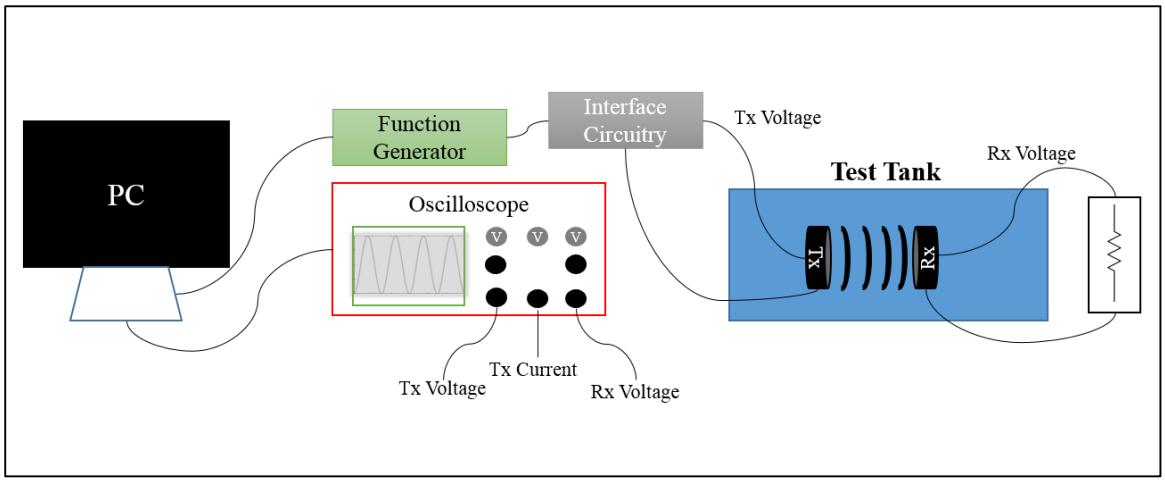

Figure 13: Experimental diagram showing the equipment used to run the frequency tuning experiment. The interface circuitry can be seen in Figure 14 while Figure 15 shows the test tank.

The probe connections to the oscilloscope and electrical schematic are shown in Figure 14. A sense resistor, $R_{sense} = 209\Omega$, was used to monitor input current and a transformer was used to increase the drive voltage from the function generator to the transmit transducer and to isolate the transmit transducer ground from the scope probe ground to prevent direct electrical coupling between the transmit and receive sides.

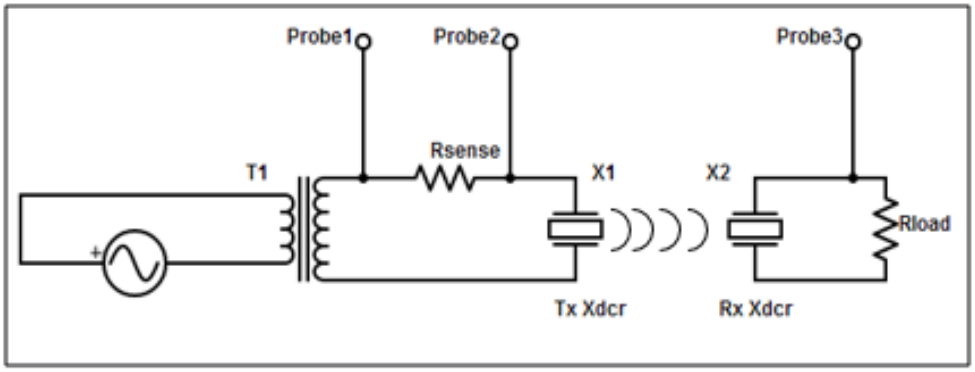

Figure 14: Schematic for circuit connections used in the experiment. Rsense is the current sense resistor, T1 is the transformer and Rload is the matched load resistance

A photograph of the experimental setup is shown in Figure 15 where the porcine tissue is sandwiched between the two transducers which are mounted in a ThorLabs cage system.

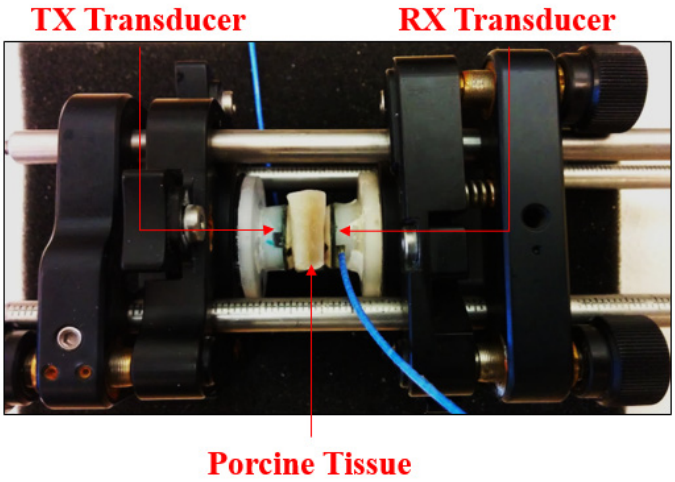

Figure 15: Experimental setup showing porcine tissue sandwiched between the transmit and receive transducers. The entire setup is housed using a ThorLabs cage system

In order to compare the frequency tuning feedback protocol performance versus that of an uncompensated ultrasonic link, an experiment was designed to compare fixed-frequency

performance versus frequency-compensated performance. For the experiment, efficiency measurements were evaluated under two conditions. For the first condition, the frequency of maximum efficiency was determined at the start of the experiment and then used consistently throughout the subsequent experiment. For the second condition, impedance phase measurements were monitored and the frequency of operation was chosen using the impedance phase minimum closest to the global optimum frequency, f_p.

Every five seconds, the efficiency under each condition was evaluated. During the experiment, the porcine tissue sample was manipulated/palpated in order to induce random changes in the effective acoustic separation between the two transducers. Figure 16 shows the 20-minute experiment where fixed-frequency performance is plotted with a dashed line and algorithm performance is shown with a solid line.

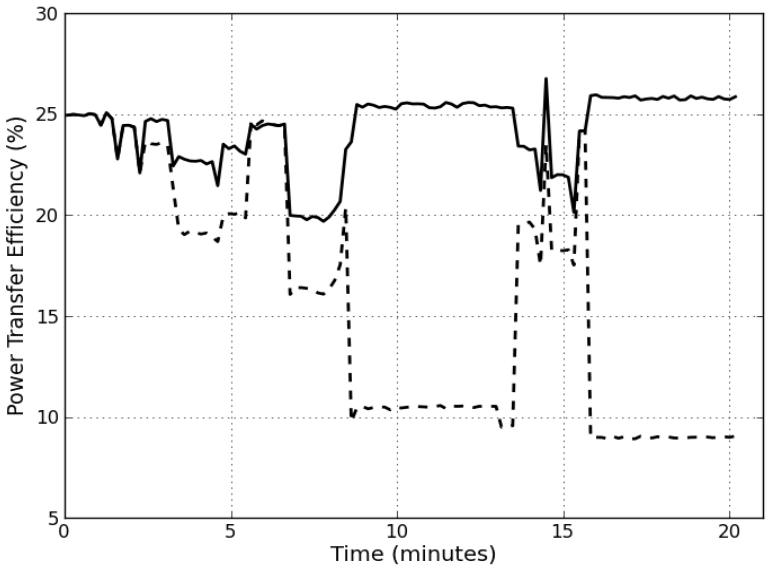

Figure 16: Power transfer efficiency achieved through a 5mm porcine tissue sample over time. The solid line represents a frequency-compensated ultrasonic link while the dashed line shows fixed-frequency performance.

Tissue manipulation events are observed to cause severe fluctuations in power transfer efficiency for the fixed-frequency system, even dropping it is low as ~8% from its initial value of ~25%. In contrast, the frequency-compensation strategy proved to be very effective keeping the power transfer efficiency above 20% over the course of the entire experiment.

Frequency-compensation is not capable of completely eliminating PTE variation in an ultrasonic link. There are other effects such as angular misalignment, lateral misalignment, and diffraction that can cause efficiency changes and cannot be removed by tuning of the frequency. In order to examine the effectiveness of frequency tuning independent of these effects, the efficiencies achieved were normalized to the maximum efficiency possible across all frequencies. Figure 17 shows the normalized results where the frequency

compensated performance is shown to stay within >97% of the maximum possible power transfer efficiency. The fixed-frequency performance fluctuates heavily and reaches a worst-case value that is only 34% of the potential maximum PTE.

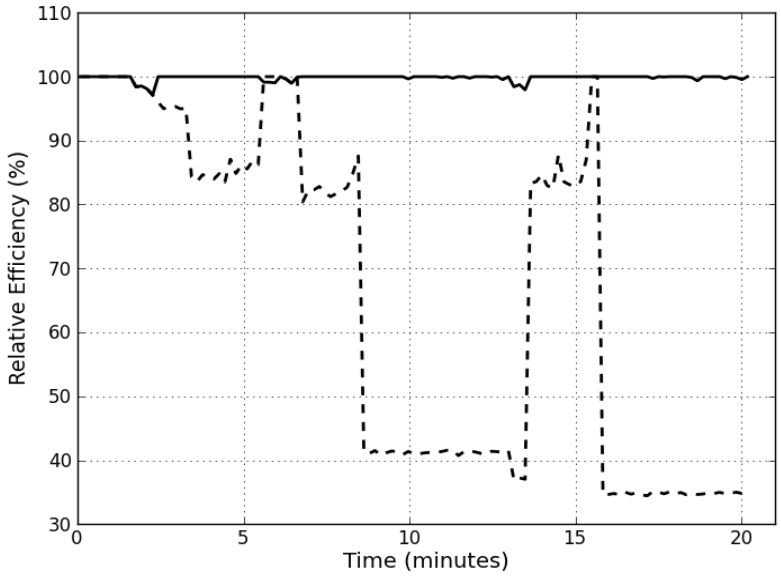

Figure 17: Normalized efficiency results for a frequency-compensated ultrasonic link (solid line) and a fixed-frequency ultrasonic link (dashed line).

Discussion

The algorithm's measured performance using a realistic experiment proves that impedance phase measurements can be used effectively to compensate for channel effects in an ultrasonic link. In addition, the measured results for a fixed-frequency system show that compensation is critical in order to maximize battery life. The presented feedback protocol makes use of only transmit-side measurements permitting its use for implants without two-way communication links. The following chapter will present the design of a high efficiency transmitter that is capable of implementing this protocol.

CHAPTER 3: RF AMPLIFIER DESIGN IN AN ULTRASONIC LINK FOR WIRELESS POWER DELIVERY TO IMPLANTED MEDICAL DEVICES

In a battery-operated ultrasound link designed for powering active implanted devices, there is a requirement for a high efficiency inverter circuit that is capable of taking the direct current (DC) supplied from a battery and converting it into RF alternating current (AC) stimulus for driving the transmitting piezoelectric element. Commonly, the DC input voltage, output voltage, waveform shape, frequency, and output power level are specified for a given inverter design. For this application the nature of the transmitting piezoelectric dictates some of the inverter requirements, such as load and frequency capability of the circuit while other parameters are more application dependent. For example, the amount of power required by different implanted devices can vary from microwatts for a cardiac pacemaker to milliwatts for a cochlear implant. In order to accommodate different loads and/or time-varying loads, we implement a burst-mode re-charging system for the ultrasonic link. Figure 18 shows a system block diagram for this power transfer protocol.

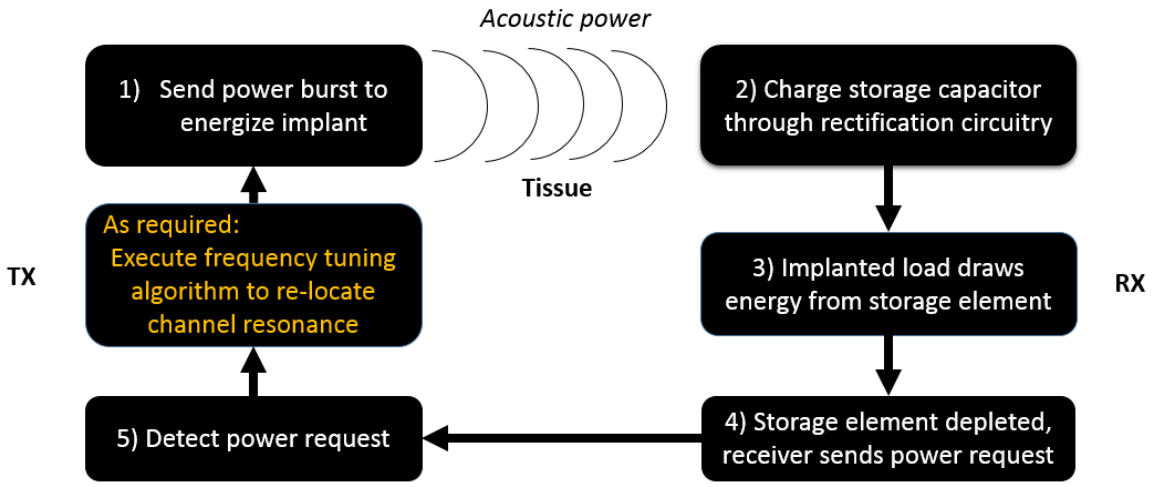

Figure 18: Proposed power transfer protocol for the ultrasonic link

On start-up, the transmit unit energizes the implanted storage element and then waits for subsequent requests for power from the receive unit. The power-request signal can be sent through a sideband link such as an RF communication link, or through the ultrasonic link itself. This mode of operation ensures that power is only sent as needed which saves power and accommodates a variety of load demands. For implanted hearing aids, there can be long periods of time where external audio levels are low and the internal storage element (battery or capacitor) will only require small amounts of energy to remain charged. Without a burst-mode power transfer protocol, the external unit must provide power continually and the external battery will be drained un-necessarily when in these situations. The transmitter can also execute a periodic frequency tuning protocol to operate at the most efficient drive frequency. The algorithm used within the design can be based on impedance phase measurements or direct measurements of input and output power versus frequency, as outlined in Chapter 2.

With implanted hearing aid devices like cochlear implants, the following requirements drive transmitter design: ***1) Size, 2) Efficiency, 3) Power level, 4) Frequency***

tuning capability, and 5) On-demand charge capability. In this Chapter, the criterion for each design requirement will first be covered. Following the descriptions, an overview of the potential amplifier designs capable of meeting the design requirements will be given. Finally, the chosen transmitter design and its full specifications will be given followed by experimental results on its performance.

Inverter Design Requirements

1) Size: It is desirable to have the inverter/transmitter electronics be as small as reasonably possible such that they can eventually be packaged into a device that can be worn comfortably by an end-user. As a result, size constraints are placed on the electronic components selected for use. This requirement rules out the use of large inductors, transformers, and other large circuit elements. One of the current state-of-the-art audio processors offered by Medel is the Amadé audio processor which measures approximately 30mm in diameter and 8.8mm in height [19]. This gives the external device a total encapsulated volume of ~6222 mm^3. A single zinc air cell is used in the design which consumes approximately 63 mm^3, thus we use a volume of ~6159 mm^3 as a point of comparison for the device being developed in this work (ultrasonic link + external circuitry).

2) Efficiency: The external unit should last an acceptable amount of time before users are required to change the device battery. Commonly, zinc air batteries are used for powering the external device. Zinc air batteries use atmospheric air for the cathode reaction giving them a high energy density and making them much lighter than other battery types. As an example, a zinc-air cell rated for 675 mAh has an overall diameter of 11.6 mm, height of 5.4 mm, and weighs 1.8 grams [20]. While device battery life will depend on the

implanted load's power requirement and the link efficiency, the transmit circuitry should be designed to be as efficient as possible. There are various figures of merit and measures of efficiency for oscillators and amplifiers. Our requirement is for > 80 % efficiency which we define as the ratio of output RF electrical power to input DC power (i.e. power driving the transducer relative to the supplied battery power).

3) Power level: The implanted device is expected to present a time-varying load as audio drive level fluctuates, and the power requirement for implanted hearing aid applications is typically in the range of a few milliwatts to tens of milliwatts [21]. The external transmitter is required to be capable of powering the load efficiently through its full range of normal impedance. Using a worst-case transducer link efficiency of 20 % and heaviest expected load demand of 30 mW, a minimum transmitter output capacity of 150 mW is required.

The ultrasonic link's maximum power is regulated by safety standards. From the Health Canada reference, *Guidelines for the Safe Use of Diagnostic Ultrasound*, to avoid inducing significant physiological effects the maximum value for the de-rated spatial peak time average intensity, $I_{SPTA.3}$, should not exceed 720mW/cm^2 [22]. The guideline is in agreement with the United States Food and Drug Administration (FDA) document, *Information for Manufacturers Seeking Marketing Clearance of Diagnostic Ultrasound Systems and Transducers* [23]. $I_{SPTA.3}$ (mW/cm^2) is the de-rated spatial-peak temporal-average intensity. In a continuous wave application, we can consider a worst case scenario in which the transmitter is always on, representing a 100 % duty cycle. For a transducer diameter of 8 mm, there is an active area of 0.50 cm^2 which places a resulting constraint on the output power. In order to comply with the maximum value for $I_{SPTA.3}$ the

transmitter's output must therefore remain below 360 mW. These two constraints place a bound on the power level:$150\ mW \leq\ P_{out} \leq 360\ mW$.

4) Frequency tuning capability: As explained in Chapter 2, we require that the transmitter have frequency tuning capability in order to compensate for channel effects and maintain maximum power transfer efficiency levels. The required tuning range is from 1.20 MHz to 1.35 MHz with the expected minimum separation of 5 mm (see Figure 11 in Chapter 2). A frequency step size of 5 kHz allows the transmitter to stay within 5% of the maximum possible power transfer efficiency value.

5) On demand charging capability: Given the power requirement variability on the receiver side, it is desirable to have the transmitter act in a 'charge-on-demand' fashion. Without such capability the transmitter would send power even when it was not needed on the receive side which wastes power and ultimately lowers operating efficiency. The size of receive side storage element (capacitor, rechargeable battery) and power required by the implant will dictate the recharge frequency.

Potential Inverter Topologies

RF amplifiers are used to convert DC power into RF power through inversion. There are six main classes of RF amplifiers: A, B, C, D, E, and F. The amplifier class that a given design falls into depends on the transistor's biasing condition, the impedance matching network used to drive the load, and the drive signal type. Class A, B and C amplifiers are quasi-linear amplifiers and can be subdivided based on their conduction

angle which represents the on-time for the switching device, or the portion of the RF cycle in which the device is conducting. The efficiency for Class A, B, and C amplifier designs tends to be lower than that of Class D, E and F because Class A,B, and C designs all spend time operating in the linear region of the transistor (somewhere between cutoff and saturation) where the transistor dissipates power. The dissipative losses in the transistor lower the amplifier's efficiency. In contrast, Class D, E, and F amplifiers operate by switching between full saturation and cutoff so that, ideally, they always have either zero drain-source voltage or zero drain current. Amplifiers in these classes are referred to as switch mode amplifiers. Importantly, this mode of operation avoids the transistor's linear/triode region where efficiencies drop. Previous researchers have shown that Class D and Class E amplifiers can be highly efficient drivers for piezoelectric devices. Ozeri et al. reported in [14] on a Class D amplifier design achieving 91.8% efficiency at a drive frequency of 650 kHz. Cheng et al. reported in [24] on a Class E amplifier design achieving 96% at a drive frequency of 41 kHz. Amplifier efficiency, as a general rule, tends to decrease with increasing frequency as switching losses and gate-drive power increase. This makes the development of efficient, high frequency, low power transmitters a significant design challenge. In order to determine whether a Class D or Class E amplifier design is best suited for the ultrasonic power link, an estimate of the loss sources for each design topology was developed.

Class D Amplifiers: A typical schematic for a Class D amplifier is given in Figure 19 for reference. Transistor Q1 and Q2 are switched on alternately at the operating frequency creating a square wave with amplitude ~Vcc on the left-hand side of inductor L1. L1 and

C1 make up a resonant tank at the operating frequency and can be used to increase the amplitude for the sinusoidal voltage provided to the load. The resonant tank also typically serves as a low-pass filter to provide a high impedance to the harmonic content contained in the square wave. It is possible to add a DC-blocking capacitor in series with the load/piezoelectric transducer in order to keep the drive signal centered on zero volts.

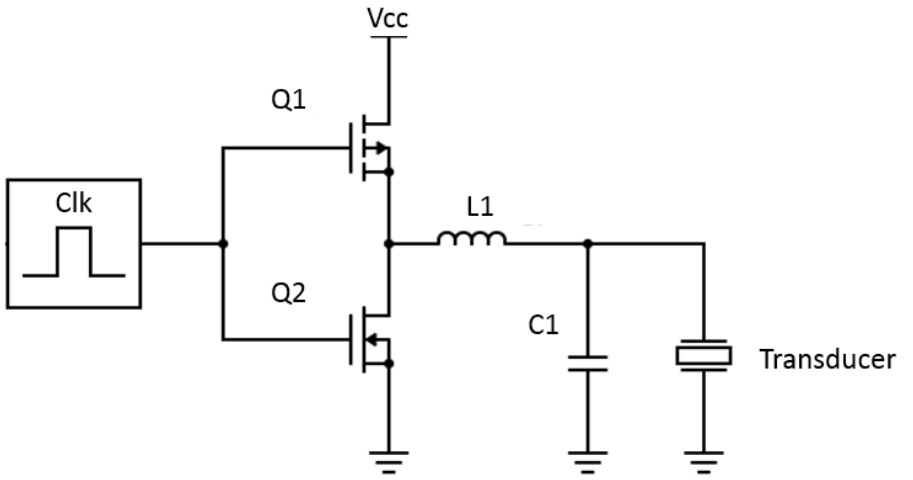

Figure 19: A Class D Amplifier driving a Piezoelectric Transducer

There are three main loss sources associated with Class D amplifiers: conduction loss, gate drive loss, and switching loss [25]. Conduction loss occurs due to the finite on-resistance of the FETs used in the amplifier which makes them non-ideal switching devices. The amount of conduction loss present in the design depends on output power, the on-resistance value, and the load value as shown in Equation (7).

$$P_{cond} = \frac{P_{out} R_{DS(ON)}}{R_{load}} \qquad (7)$$

The next loss source, shown in Equation (8) is associated with driving the gates of the FETs. P_{gd} is the power lost to gate drive and depends on the FET's gate charge, Q_g, the gate-source voltage, V_{gs}, and the operating frequency, f_{op}.

$$P_{gd} = 2Q_g V_{gs} f_{op} \qquad (8)$$

Finally, there are switching losses associated with the FETs in the amplifier which can be calculated using Equation (9). C_{oss} is the FET's output capacitance, V_{cc} is the supply voltage, I_d is the RMS drain current, T_{on} is the turn-on delay, and T_{off} is the turn-off delay.

$$P_{sw} = C_{oss} V_{cc}^2 f_{op} + I_d V_{ds} f_{op}(t_{on} + t_{off}) \qquad (9)$$

Class E Amplifiers: A typical schematic for a Class E amplifier is given in Figure 20 for reference. In the schematic, a battery supplies DC voltage and current to the circuit through an RF choke inductor, L1. The inductor is sized such that the AC current ripple on the DC supply is negligible. A driving clock signal (CLK), turns the switch Q1 on and off at the desired operating frequency. A shunt capacitance (C1) can be assumed to include the choke's parasitic capacitance as well as the transistor's output capacitance. With the switch in the ON state, capacitor C1 becomes shorted to ground and a resonant circuit is formed by C2, L2, and R1. When the switch is in the OFF state, the resonant circuit includes C1 in series with C2, L2, and R1.

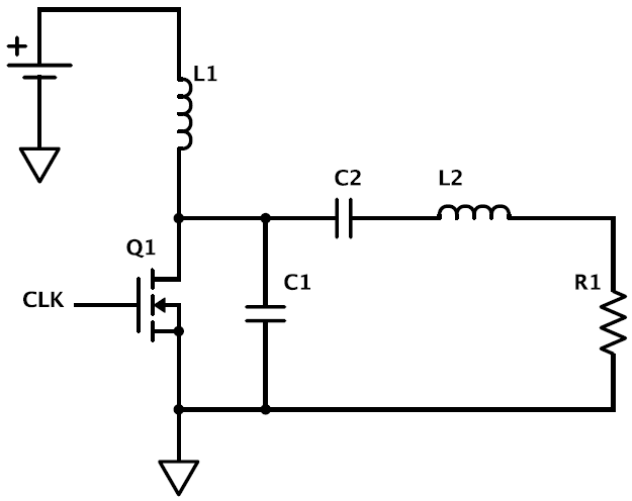

Figure 20: A typical Class E Amplifier

There are two main loss sources associated with Class E amplifier designs, gate-drive loss and conduction loss. For a class E amplifier, the gate-drive loss is given by Equation (10), which is half of the gate-drive loss for a Class D amplifier since only one switching device is used in the Class E design.

$$P_{gd} = Q_g V_{gs} f_{op} \qquad (10)$$

The conduction loss in a class E amplifier exists due to non-zero on-resistance of the FET Q1. Conduction loss is approximated using Equation (11) which is equivalent to the conduction loss in a Class D amplifier.

$$P_{COND} = I_{RMS}^2 R_{DS(On)} \qquad (11)$$

The final potential loss-source for a Class E amplifier is switching loss. The switching loss associated with the transistor in Class E amplifiers is given by Equation (12) and depends on the transistor output capacitance and load capacitance, C, the voltage being switched, V_{DS}, and the frequency of operation, f. Switching loss increases linearly with frequency and often represents a dominant loss source for amplifiers. The strategy adopted in Class E designs, is to design the amplifier's resonant load network such that the drain-source voltage is nominally zero just prior to turning on. Referring back to Figure 20, C2 and L2 block harmonics and DC from the load, meaning their current is sinusoidal at the operating frequency. The DC choke inductor L1 is sized such that it only conducts DC current. Current gets commutated between C1 and Q1 depending on the state of Q1. With Q1 on, the voltage across C1 is forced to zero and current flows through the switch. With Q1 off, the current flows through C1. Through amplitude and phase adjustment of the current sinusoid, the capacitor's stored energy can be set to zero just prior to transistor Q1 turning on (meaning the drain-source voltage is zero). It is also possible to ensure that the current waveform is zero just prior to transistor Q1 turning on. These two design characteristics are referred to as zero-voltage switching and zero-derivative switching respectively, and ensure that power lost to switching (due to simultaneous drain-source voltage and drain-source current) is nominally zero. Zero-voltage switching operation eliminates the loss given in Equation (12).

$$P_{SW} = \frac{1}{2} C V_{SW}^2 f \qquad (12)$$

Class D versus Class E: It is possible to design Class D amplifiers to operate in a zero-voltage switching fashion as well, which effectively brings their switching loss also close to zero. However, the Class E amplifier design remains a more efficient topology for the ultrasonic power link owing to its use of a single switching device which results in half of the required gate-drive power when compared with the Class D amplifier topology.

Class E Amplifier Design for the Ultrasonic Power Link

With a chosen inverter/amplifier topology, we can begin the process of setting the main design parameters. For implanted hearing aids, power is typically supplied by a rechargeable or disposable battery. Zinc-air cells, which have a nominal 1.2V output, are often chosen due to their high energy density. Unfortunately there are very few standard integrated circuits (ICs) capable of operating from a 1.2V supply. More commonly ICs require a 3.3V or 5V supply. In order to boost the voltage from 1.2V to either 3.3 or 5.0 V, a high efficiency synchronous boost regulator can be used.

The ultrasonic link has a frequency-dependent power transfer efficiency spectrum dictated by the resonant cavity formed between the two transducers [1],[2], [3]. Operation at frequencies for which the efficiency is maximal requires that the drive circuit be able to generate a tunable frequency between 1.20 and 1.35 MHz. Ultrasound safety limits place an upper bound on the output power of the device of 360 mW. A burst-mode power delivery approach dictates a lower bound of 150 mW in order to achieve the required time-averaged delivered power. Finally, at the acoustic resonance of the channel formed between the two transducers, the impedance looking into the transmit transducer is 500 Ω and real. The

desired efficiency metric for the amplifier/inverter is >90% in order to maximize battery life. The design parameters are summarized in Table 1 below.

Design Parameters	
DC supply level	3.3 or 5.0 V
Frequency	1.20 – 1.35 MHz
Output power	150 mW ≤ Pout ≤ 360 mW
Duty cycle	50%
Nominal load impedance	500 Ω
Desired efficiency	> 90 %

Table 3: Amplifier design parameters for the ultrasonic transcutaneous energy transfer link

For ideal operation of the class E amplifier circuit shown in Figure 20, there are four specific equations for determining the component values of the resonant circuit. The supply voltage - V_{cc}, output power - P_{out}, and load resistance - R_s, are all related by Eq. (13) while Equations (14), (15), and (16) are for finding C1, L2, and C2 respectively. X_{C1} and X_{C2} are the reactances of capacitors C1 and C2, and Q_L is the loaded quality factor of inductor L2. Equations (13) through (21) below, are from reference [26], and optimize the circuit design such that simultaneous voltage and current in the switching transistor is avoided.

$$R_s = \frac{8}{\pi^2 + 4} \frac{V_{cc}^2}{P_{OUT}} \approx 0.58 \frac{V_{cc}^2}{P_{OUT}} \qquad (13)$$

$$X_{C1} = \frac{1}{\omega C_1} = \frac{\pi(\pi^2 + 4)R_s}{8} \approx 5.45 R_s$$

(14)

$$X_{L2} = \omega L_2 = Q_L R_s \tag{15}$$

$$X_{C2} = \frac{1}{\omega C_2} = \left[Q_L - \frac{\pi(\pi^2 - 4)}{16} \right] R_s$$

$$X_{C2} \approx (Q_L - 1.1525) R_s \tag{16}$$

The load impedance looking into the transmit piezoelectric transducer is approximately real and equivalent to a 500 Ω which is ~20 times greater than the load value defined by Eq. (13) using Vcc=3.3V and Pout=250mW. A matching circuit is therefore necessary for the design to match the load impedance to that set by Eq. (13). A tapped capacitor impedance matching resonant circuit can be added to the network in order to transform the piezoelectric load impedance down to the nominal value of 20Ω. The matching network and its equivalent circuit are shown below in Figure 3.

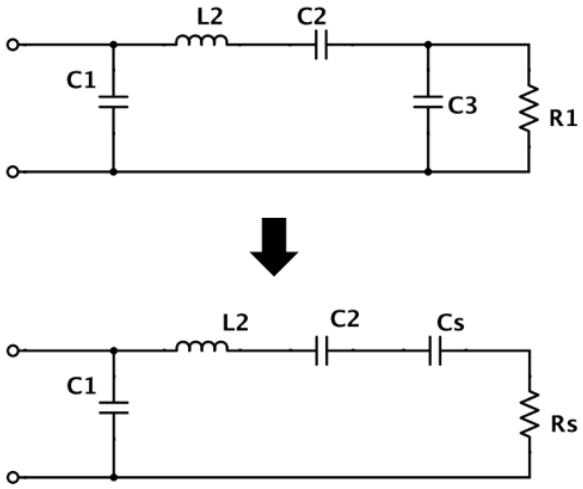

Figure 21: Impedance matching circuit and its equivalent circuit. The tapped capacitor C3 provides downward impedance transformation.

The reactance factor for the matching circuit can be calculated using Eq. (17) below and gives a value of 4.358.

$$q = \sqrt{\frac{R_L}{Rs} - 1} \qquad (17)$$

The reactance factor can then be used to determine the size of capacitor C3 through Eq. (18) resulting in a capacitance of 1085 pF.

$$X_{C3} = \frac{1}{\omega C_3} = \frac{R_L}{q} \qquad (18)$$

In order for the correct value of C2 to be calculated, the series combination of C2 and Cs must be used.

$$\boldsymbol{X_{Cs} = qRs}$$

$$\boldsymbol{X_{C2} = \frac{1}{\omega C_2} = X_C - X_{CS}}$$

$$\boldsymbol{X_{C2} = R_L\left[Q_L - \frac{\pi(\pi^2 - 4)}{16} - q\right]} \qquad (19)$$

With $R_L = 500\ \Omega$, $q = 4.358$, Q_L is set to a value of 7 and $C2 = 3312\ pF$. Inductor $L2 = 21.95\mu H$ through Eq. (15) and $C1 = 912\ pF$ through (14).

Many transducers, when driven at their mechanical resonant frequency are modelled as a clamped capacitance in parallel with a resistance (the transducer's equivalent acoustic resistance). In these cases, capacitor C3 should be sized accordingly given the parallel combination of C3 and the clamped transducer capacitance [24].

The final calculation for the inverter is to determine an appropriate size for the RF choke inductor, L1. From the literature on Class E amplifiers [26], a suggested minimum choke inductance can be found using Equation (20) which ensures that the maximum peak to peak current ripple is < 10%. This results in a minimum choke inductance of 327 µH.

$$L_{Min} = 8.67\frac{R}{f} \qquad (20)$$

The ESR for the chosen inductor should be minimized in order to minimize the power loss in the inductor. The power lost to the inductor can be calculated using:

$$P_{InductorLoss} = \frac{ESR_{Inductor} P_{out}}{R} \quad (21)$$

Class E Amplifier Simulation and Testing

In order to validate the proposed amplifier design, circuit simulations were performed using LTspice – a free circuit simulation tool. First, the circuit efficiency was evaluated across the intended operating frequency range. Two different efficiencies were calculated, one taking into account only the conduction and switching losses (Eq. (22)) and the second also including losses associated with the gate drive circuitry (Eq. (23)). Figure 22 shows the testing results where the diamond data markers show the efficiency as calculated by Eq. (22) and the square data markers are calculated using Eq. (23).

$$\eta = \frac{P_{out}}{P_{Battery}} \quad (22)$$

$$\eta = \frac{P_{out}}{P_{Battery} + P_{GateDrive}} \quad (23)$$

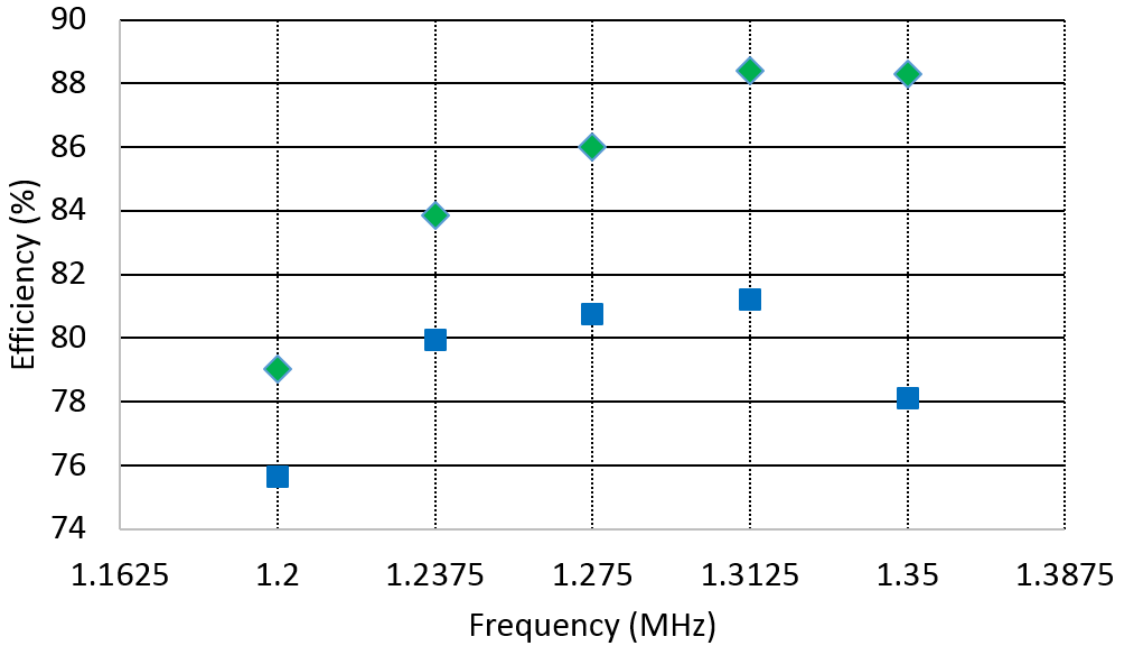

Figure 22: Efficiency versus frequency for the designed Class E amplifier. Green diamond markers represent the ratio of RMS output power to RMS DC supply power. Blue square markers represent the system efficiency and include power lost to driving the gate of Q1.

The average gate drive power associated with driving the N-channel FET (DMN26D0UT) was between 17-19 mW and is shown to incur a system loss between 4 % and 10 % depending on the operating frequency and output power level. The rest of the system loss is attributable to switch loss, and non-zero equivalent series resistance (ESR) in the inductors. While the class E amplifier is designed for zero-voltage switching conditions, real FETs have a finite on-resistance meaning the drain cannot be completely clamped to GND when the drain current is non-zero which results in some conduction loss. Vds values of 100-200 mV can result in average (IdsVds) products of approximately 15-25mW. Figure 23 shows the simulated drain-source voltage and drain-source current.

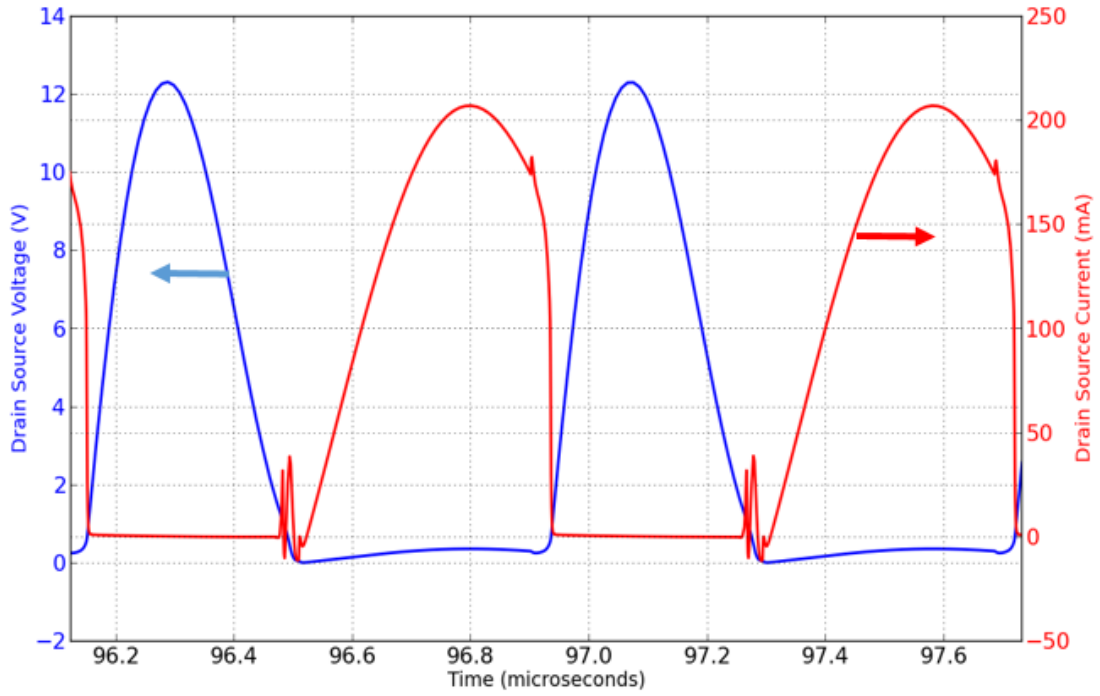

Figure 23: Transistor Q1 simultaneous drain and current waveforms during switching. Vds does not clamp fully to zero resulting in some switching loss. Arrows indicate y-axis for each waveform.

A conference proceedings on this topic (Class E RF amplifier designs for use in ultrasonic links) was published in the 2015 IEEE Canadian Conference on Electrical and Computer Engineering.

Efficiency Improvement through FET selection: In the preceding section, the loss sources associated with the Class E amplifier were narrowed down to gate drive power and simultaneous products of Vds and Ids. The power dissipated across the switching device (VdsIds) and the power drawn for gate-drive are both related to the chosen transistor within the design. A common metric used to evaluate a given transistor is "Figure of Merit", (FOM). The FOM, equal to the product of gate charge (Qg) and on-resistance ($R_{DS(On)}$), relates to the device technology. A low FOM is particularly important for achieving high

efficiency at high frequencies. While within a particular technology gate charge can be traded off against on-resistance, their product is roughly constant across devices. In 2009, Efficient Power Conversion Corporation (EPC) introduced the first enhancement mode gallium nitride (eGaN) transistor and demonstrated that eGaN based devices can be made with Figure of Merit values that are 4-5 times lower (better) than the best silicon MOSFETs [27].

Given this advantage, we hypothesized that eGaN FETs would drive better performance in UTET applications than traditional silicon FETs that had been used previously. Simulations were performed with the same Class E amplifier as above using a gallium nitride FET in place of the silicon MOSFET. eGaN FET device parameters are available for download and the EPC8002, an eGaN FET with a specified total gate charge of 141pC (Vds = 32.5V, Id = 1A) and specified maximum on-resistance of 530mΩ [28], was used. Below, Figure 24 shows the amplifier efficiency versus frequency with the silicon FET data for comparison. The peak efficiency is 93% using the EPC8002 compared to 81% using a high performance silicon MOSFET. The efficiency performance across the desired frequency range is also improved, staying above 85% over the entire range.

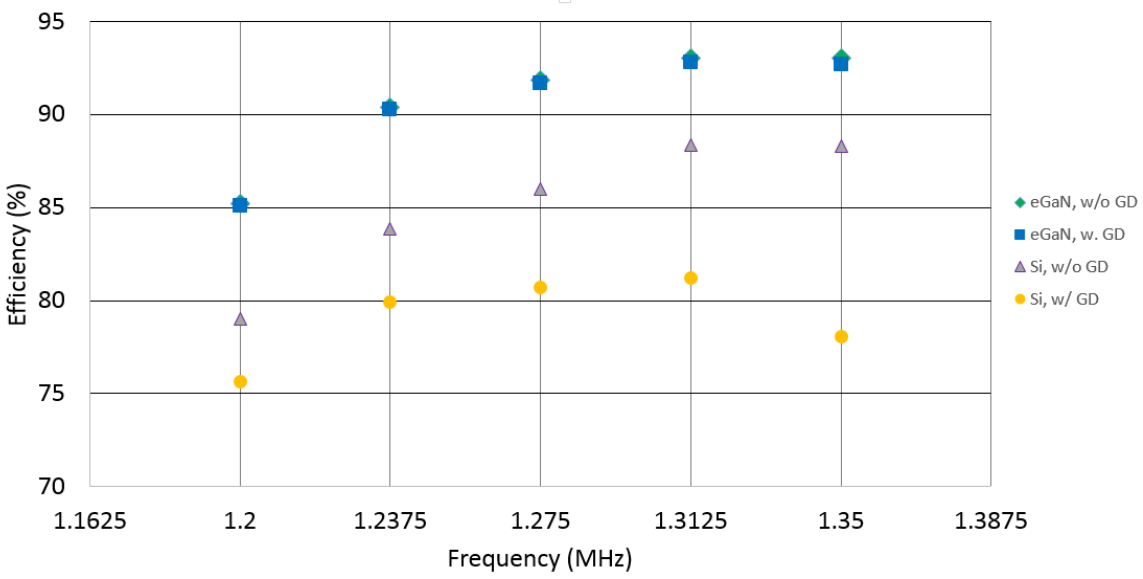

Figure 24: Efficiency versus frequency for the designed Class E amplifier comparing an enhancement mode gallium nitride field effect transistor (eGaN FET) versus a silicon MOSFET. Green diamond and purple triangle markers represent the ratio of RMS output power to RMS DC supply power, using a 500Ω load. Blue square and yellow circle markers represent the system efficiency and include gate drive (GD) power. The peak efficiency reaches 93% while gate-drive power has virtually no effect on efficiency. The efficiency improvement is attributable to the eGaN FET's Rds-on value of 530mΩ and total gate charge of 141pC.

Output Power: Simulations were also run in order to determine the variation in output power across frequency for the amplifier design. The green diamond markers in Figure 25 show the measurement result. Output power decreases linearly with frequency for the design. This can be attributed to the impedance matching network response which presents an increasing impedance to the amplifier as frequency is increased.

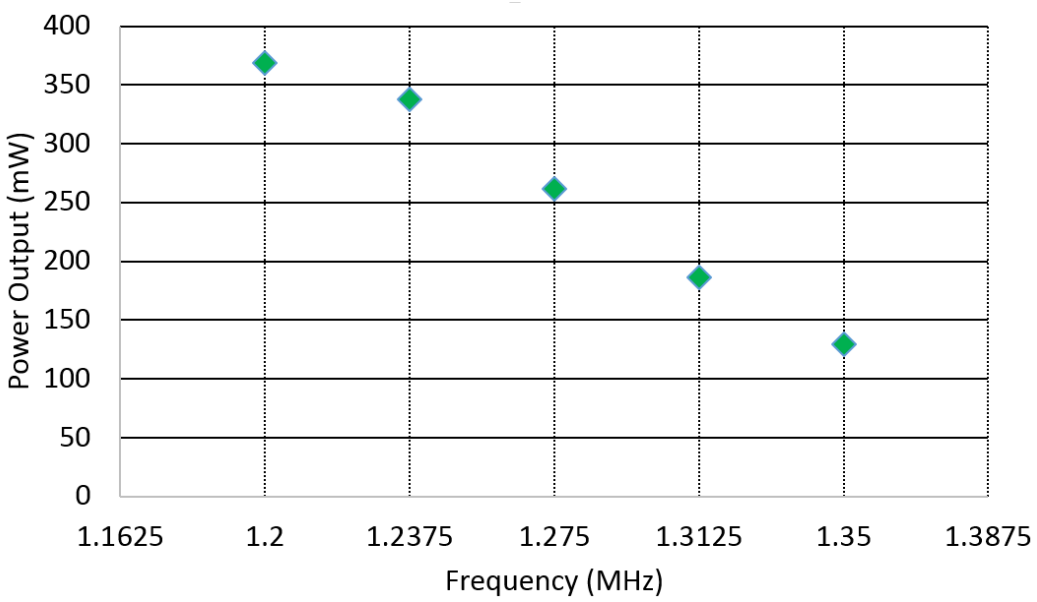

Figure 25: Output power versus frequency. The green markers indicate power delivered to a resistive load of 500Ω across the designed frequency range for the ultrasonic power link.

As mentioned earlier in the Chapter, we require that the power levels fall within the range: $150mW \leq P_{out} \leq 360\ mW$. The measurement results shows that for f=1.35 MHz, the minimum target output power requirement is not quite met. In order to maintain power levels between $150mW \leq P_{out} \leq 360\ mW$, a potential design solutions is to use an adjustable step-up DC-DC regulator, along with circuitry for monitoring input power to the amplifier. With these circuit components in place, a microcontroller can increase the DC supply voltage as needed to ensure sufficient power delivery across the entire frequency range. The frequency-dependent output power will also be managed through duty-cycle control in the burst-mode power transfer protocol.

The final simulation for the amplifier design was a load-value sweep to investigate the efficiency performance over a range of load impedances. Figure 26 shows the measurement

result and the efficiency reaches a peak level between 90-92% for a load impedance range of 300-600 Ω. Lowering the load value results in sharp decrease in efficiency levels, while increasing the load is less detrimental from an efficiency perspective. Smaller loads result in lower output powers making fixed loss sources, such as gate-drive power, more significant.

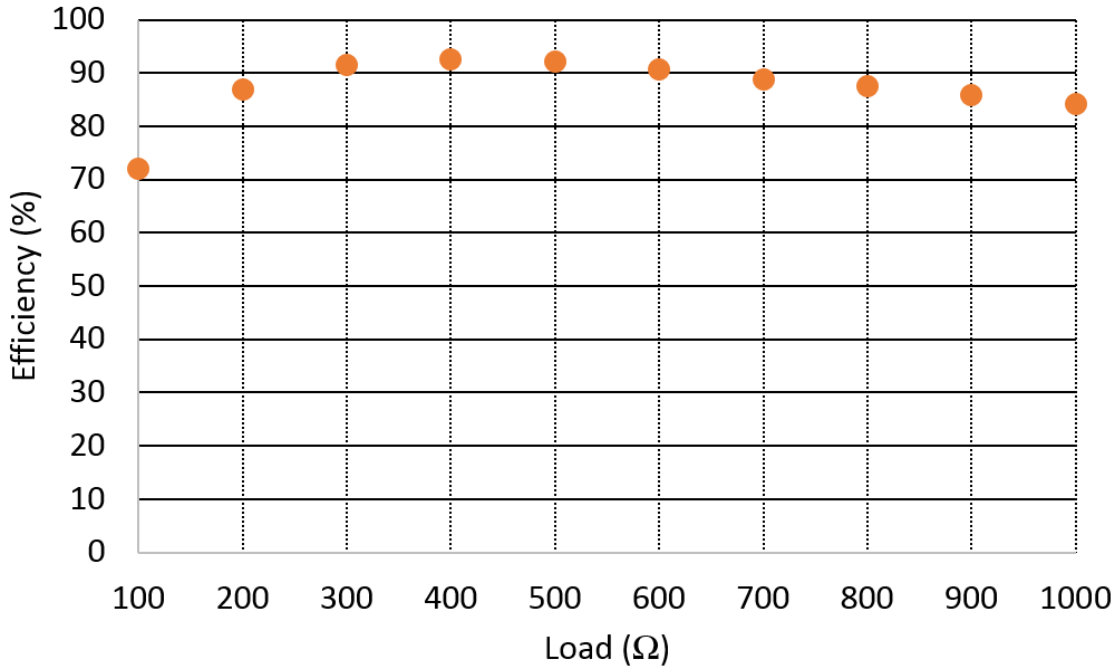

Figure 26: Efficiency versus load resistance for the Class E amplifier at 1.275 MHz.

Class E Amplifier Experimental Results

Following the circuit simulations using LTspice, a printed circuit board (PCB) was designed and populated for the Class E amplifier in order to characterize its performance using real circuit components. The first measurement performed on the circuit was an assessment of efficiency versus load. For this measurement, the following circuit setup shown in Figure 27 was used. A current sense resistor, R1, allowed for measurement of the

input current using node voltages Vs and Vin. The input power is defined as the product of the input voltage and current as: $P_{in} = V_{in}I_{in}$, while the output power is defined as: $P_{out} = V_{rms}^2/R_2$, where V_{rms} is the RMS voltage measured across the load resistance R_2. In order to characterize the efficiency versus load, a potentiometer was used for R_2. The efficiency for the designed circuit reaches a peak level of >92% and efficiency levels > 88% for a load impedance range of 169-455Ω.

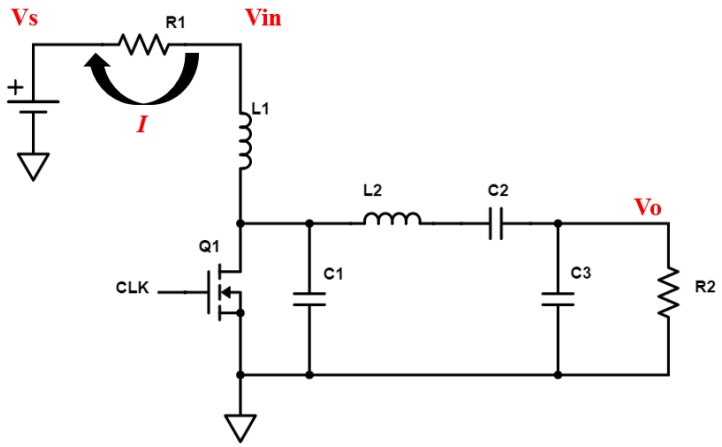

Figure 27: Circuit setup for characterization of the designed Class E amplifier

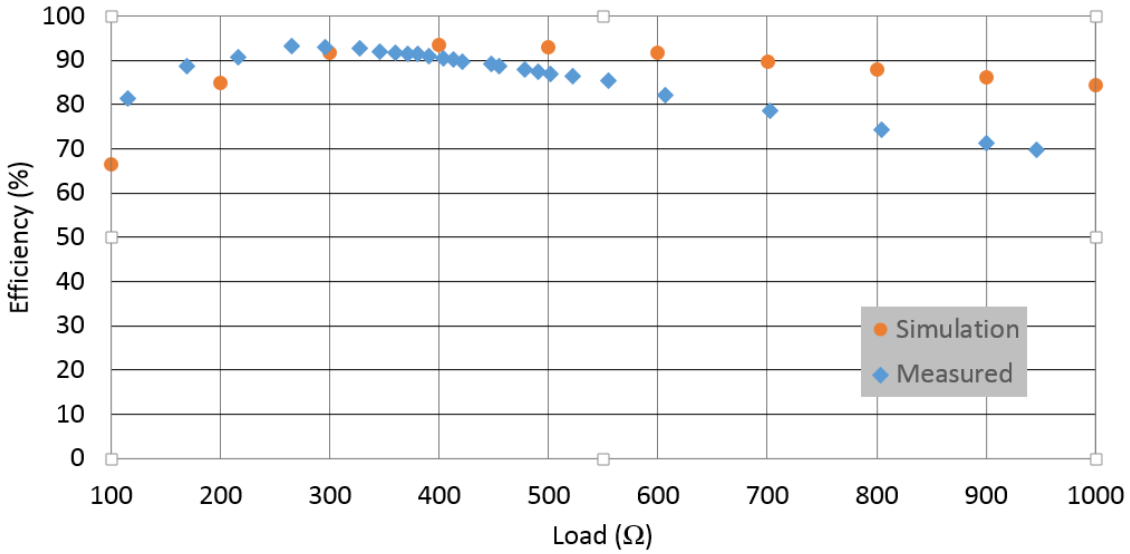

Figure 28: Efficiency versus Load value for the Class E amplifier

In the design of the Class E amplifier, first the required series resistance is calculated, which is a function of supply voltage and output power, as illustrated earlier in Eq. (13). When investigating the relationship for the measurement data using this same equation, it was found that the design-point is close to ideal for the load value of 266 Ω, while above this load value, the series resistance (calculated using measured output power and supply voltage) decreases and no longer satisfies the idealized zero-voltage switching conditions. The efficiency spectrum was then measured and Figure 29 shows the measured and simulated results which are within 5 percentage points of one another for each measurement/simulation pair.

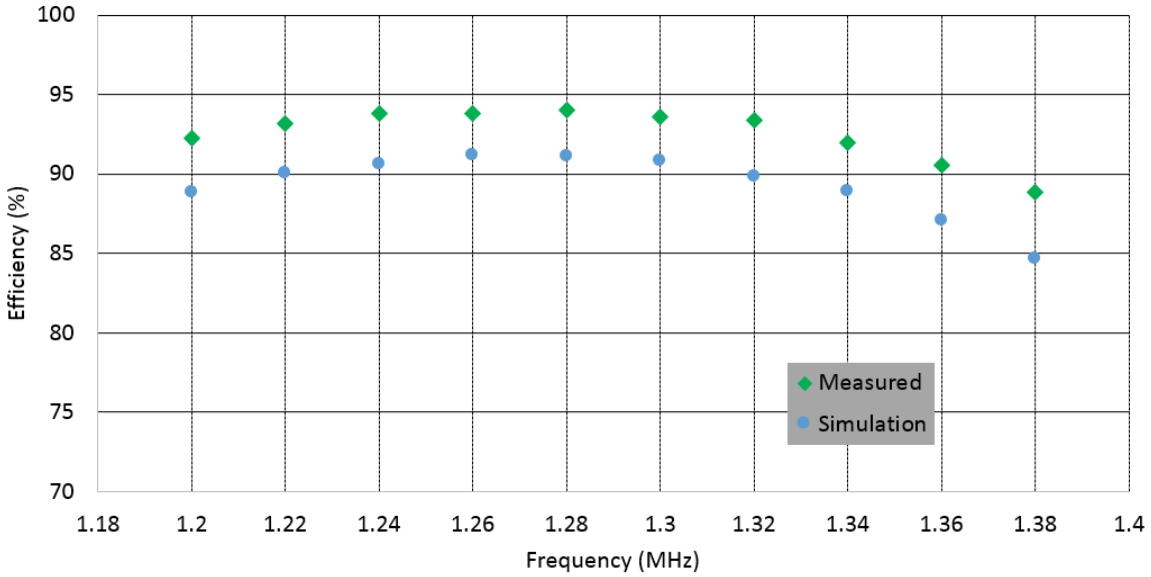

Figure 29: Efficiency versus Frequency for the Class E amplifier

Finally, the output power was characterized for the Class E amplifier versus simulation. Figure 30 shows the measurement result which shows excellent agreement between simulation and measurement. The measured data is within 10% of the simulated data over the entire measurement range.

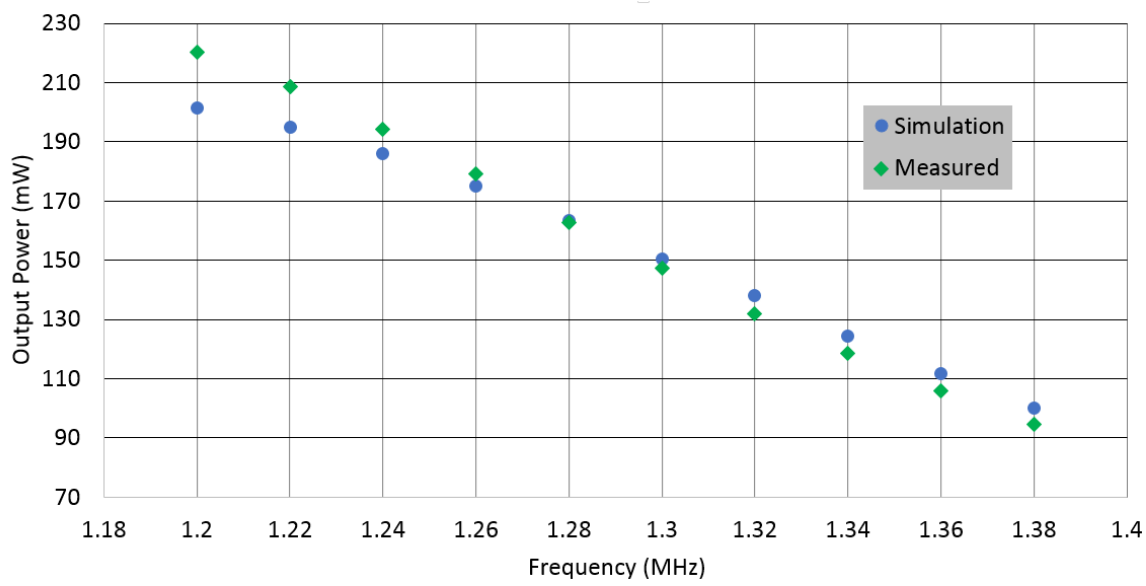

Figure 30: Output power versus frequency for the Class E amplifier

Class E Amplifier Design Assessment: The simulated results show that the Class E amplifier design is extremely well suited for the ultrasonic power link. The design can now be evaluated against the criteria set at the beginning of the chapter for the inverter/amplifier. In terms of size, the designed circuit's largest components are the two inductors used in the design (RF choke inductor L1 and resonant inductor L2). However, the required inductor values are available in surface mount packages that measure 6.6 x 4.45 x 2.92 mm (L x W x H) and can fit easily into a behind the ear style hearing aid case. One of the assembled PCBs is shown below in Figure 31.

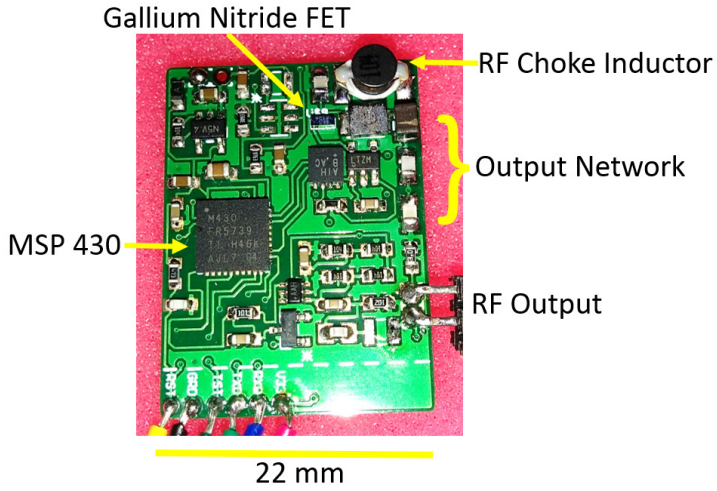

Figure 31: Assembled RF Amplifier PCB featuring a high efficiency Class E amplifier designed to drive the ultrasonic link

In terms of circuit size, the featured design is highly compact with all the components taking up a total volume < 200 mm^3. The ultrasonic link and amplifier components together give a total estimated volume under 400 mm^3, while the Amadé audio processor electronics are estimated at ~6159mm^3, although the Amadé audio processor also contains more functionality. In terms of amplifier efficiency, the proposed design operates with a peak efficiency of 93% and efficiency levels > 90 % over the required frequency

range. With respect to power level, the circuit is capable of meeting the minimum required output across the required frequency range with the use of an adjustable DC-DC converter. The amplifier also meets the required specification for frequency tuning capability. In order for on-demand charge capability, the amplifier can be enabled/disabled by switching the DC-DC converter connected to the amplifier's choke inductor ON/OFF, or by disabling the drive signal connected to the switching transistor in the amplifier. Overall, the frequency-tunable Class E amplifier is an excellent choice for powering miniature battery operated ultrasonic links.

CHAPTER 4: HIGH EFFICIENCY RECTIFICATION & BATTERY-CHARGING IN ULTRASONIC LINKS FOR WIRELESS POWER DELIVERY TO AIMDs

On the implanted side of an ultrasonic power link, there is a requirement for high efficiency rectification electronics that are capable of taking the receive transducer's AC energy and converting it into a usable DC supply. Previous researchers such as Ozeri et al [9] and Mazzilli et al [29], have previously reported on rectifier designs for use in ultrasonic links and achieved rectifier power conversion efficiencies of 88.5% and 82.45% respectively. The main design challenges in rectifying the signal from a receive transducer include: 1) presenting a conjugate impedance match to the transducer and 2) minimizing power loss due to forward diode conduction. The system components on the receive side typically include a rectifier circuit, an energy storage element such as a rechargeable battery or capacitor, and an implanted load that draws power. For the implanted hearing aid intended to be powered by our ultrasonic power link, a regulated 3.3V or 5V supply is required. In order to provide this DC supply, a high efficiency DC-DC buck or boost switching converter can be used. Figure 32 shows a potential block diagram for the energy conversion process. On the far-right, a variable resistance is shown to depict the time-varying power required by the implanted electronics. Two of the key requirements for the receive side circuit are that it be small and efficient.

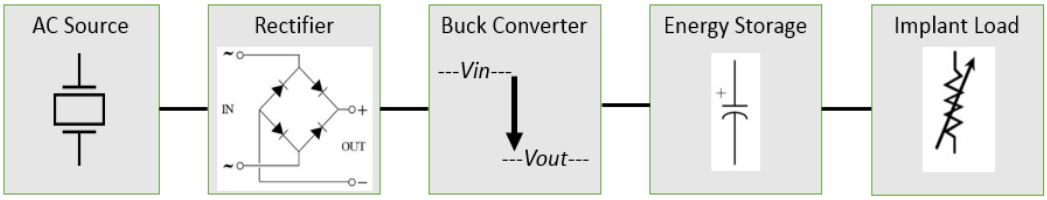

Figure 32: System block diagram showing components that could be used on the implant side of an ultrasonic power link for implanted medical devices

Conjugate Impedance Matching

In an ideal ultrasonic power-transfer scenario, the receive side transducer is connected to circuitry that provides an input impedance equal to the receive side transducer's complex conjugate (satisfying the maximum power transfer theorem). For a piezoelectric element, the impedance is frequency-dependent; as such, the requirement for a conjugate impedance match could call for a resistive, inductive, or capacitive termination. However, experimentally in this work, frequency tuning is used in order to operate both the transmit transducer and receive transducer at a point where the frequency-dependent reactance is nearly zero (i.e. the absolute value of the impedance phase angle is < 20 degrees while the magnitude is > 300 Ω). In this scenario, a complex conjugate match provides only marginal benefit (< 5% improvement in PTE) when charging a capacitor through a full-wave rectifier. In the developed circuitry we forego the use of complex conjugate impedance matching for this reason.

Rectification

One of the simplest, and most common rectifier designs is that of a full-wave rectifier, where four diodes are used in the rectification process. The schematic shown in

Figure 33 shows a full-wave bridge rectifier providing energy to a resistive load, R1. During positive half-cycles of the input waveform, diodes D2 and D3 conduct current while diodes D1 and D4 block current flow. On the negative half cycle, the opposite conduction occurs with diodes D1 and D4 conducting. This diode-action results in unidirectional current flow across the load resistance R1. A filter capacitor is typically placed in parallel with R1 in order to provide a smooth DC supply. However, the simplified schematic shown in Figure 33 was used in order to generate initial measurements of the efficiency for full-wave rectification.

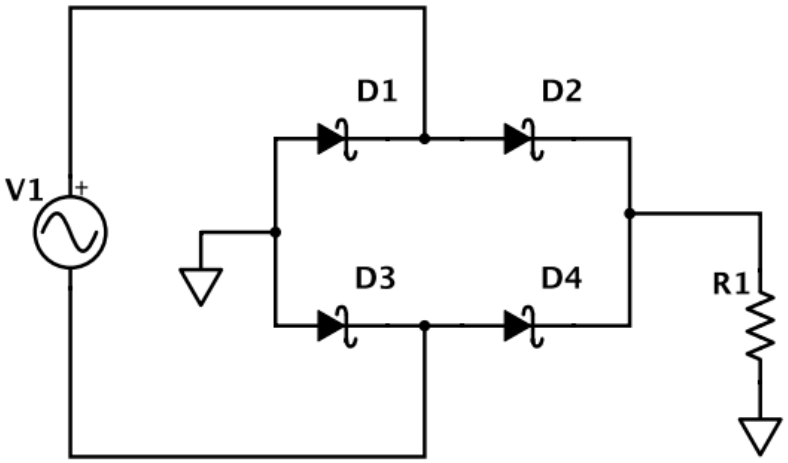

Figure 33: Schematic used in LTspice for testing efficiency of the full-wave rectification process

For a high-frequency rectifier circuit, the chosen diode should have: a low junction capacitance, a low forward voltage drop, and a low reverse recovery time. The diode must also be rated above the maximum reverse voltage expected in the circuit. With Schottky diodes, the reverse recovery time (when the diode switches from a conducting to non-conducting state), is essentially instantaneous because the device has nothing to recover from being a majority carrier device [30]. In conventional PN junction diodes, the reverse

recovery time is a function of minority carrier recombination while for Schottky diodes, the reverse recovery time is mainly present due to junction capacitance. In general, as the forward voltage drop is optimized (lowered) for a given Schottky diode, it's reverse leakage current tends to increase. The reverse leakage currents for low-power Schottky diodes (rated for < 100mA average rectified current) are on the order of nano-Amps to micro-Amps making the overall loss due to reverse leakage insignificant. The junction capacitance values are also extremely low (i.e. < 35pF at 1 MHz), making Schottky diodes extremely well suited for high efficiency, high frequency rectifier applications.

LTspice was used in order to simulate the efficiency of full-wave rectifier circuits using different Schottky diodes. Power transfer efficiency curves were measured (at 1 MHz) versus input amplitude provided by the voltage source (V1 in Figure 33) and the simulation results are summarized in Figure 34.

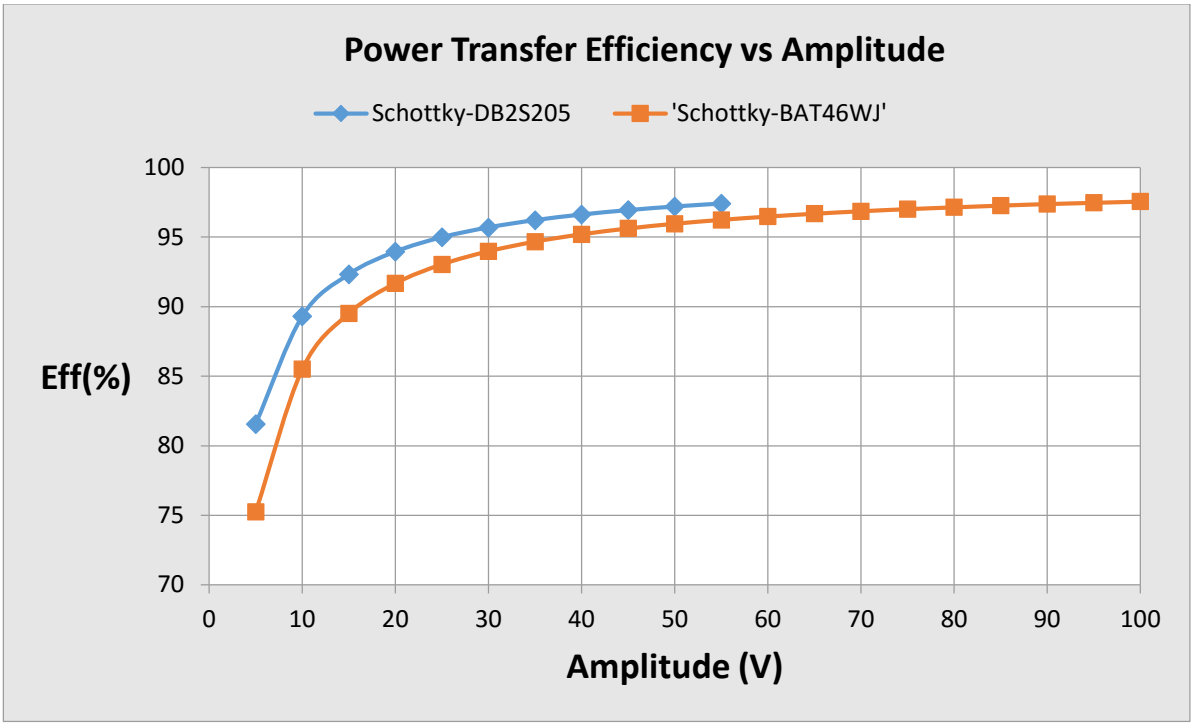

Figure 34: Efficiency versus input amplitude for 3 separate full-wave rectification circuits using different diodes. The breakdown voltage for the DB2S205 [31] diodes is 28V so the maximum amplitude was limited to < 56 volts for the DB2S205-based rectifier.

The power transfer efficiency was calculated using Eq. (24) by taking the ratio of average output power, $P_{Out(Avg)}$, to average input power, $P_{In(Avg)}$, over a span that covered >200 RF cycles.

$$\eta = \frac{P_{Out(Avg)}}{P_{In(Avg)}} \qquad (24)$$

The overall trend for each full-wave rectifier circuit tested shows that higher input amplitudes yield higher power transfer efficiencies. The efficiency increases with input amplitude as the ratio of signal level to forward bias voltage of the diode increases. In the simulation, the full wave rectifier circuit using Panasonic Schottky (DB2S205) diodes [31] outperformed the BAT46WJ diode [32] based rectifier. This occurs because the DB2S205 has a lower forward voltage drop for a given amount of current. The junction capacitance was modelled as 31pF for the DB2S205 and as 35pF for the BAT46WJ; these capacitances lead to power loss values less than a few milliwatts.

While the above simulation is useful for rectifier selection, the complete circuit will also include a filter capacitor at the output of the rectifier bridge such that a DC voltage can be developed and then connected into a DC-DC converter stage. The schematic in Figure 35 was used to generate efficiency curves versus charging time for the full wave rectifier circuit providing energy to a storage capacitor, C1. It can be reasonably expected that the power transfer efficiency for the full-wave rectifier will have a time-dependent aspect to it as the output capacitor (C1) charges up to its steady state value. This is due to the If-Vf characteristic of the Schottky diode which has less loss when operating with lower forward currents.

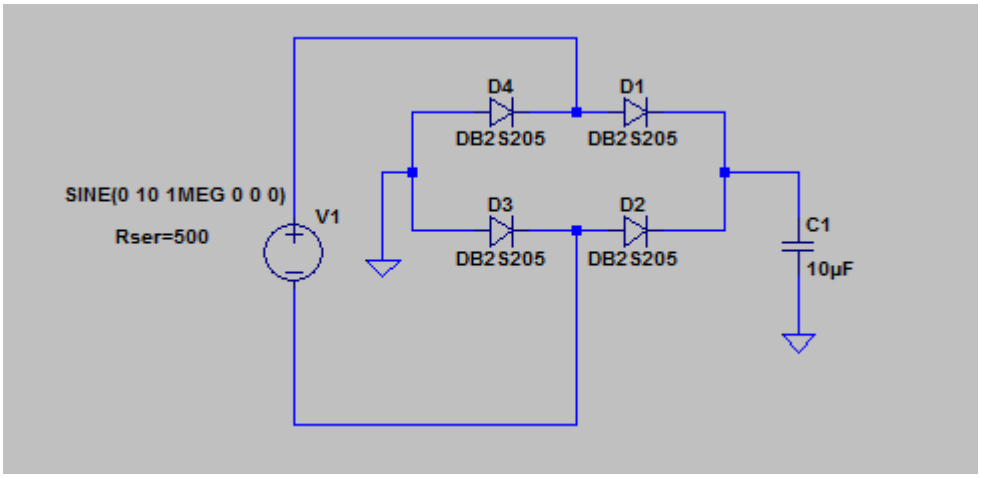

Figure 35: Rectifier and filter capacitor stage in LTspice for transient analysis

The efficiency for each simulation was calculated using Eq. (25), where E_{C1} represents the energy stored on C1 at the end of the simulation, and $\int_0^T |P_{in}|$ is the integrated energy provided by the source V1 over the simulation time. The output impedance of the receive-side transducer is assumed to be 500Ω real and is included in the sinusoidal source.

$$\eta = \frac{E_{C1}}{\int_0^T |P_{in}|} \qquad (25)$$

The energy on capacitor C1 was found using Eq. (26) below, where $C = 10\ \mu F$, and V is the RMS voltage on the capacitor at the end of the simulation .

$$E = \frac{1}{2}CV^2 \qquad (26)$$

In Figure 36, the time is represented in an RC time constant format in order to make the results insensitive to output impedance and filter capacitance value. For the circuit, $\tau = 5ms$, and N represents the multiplying factor associated with each simulation.

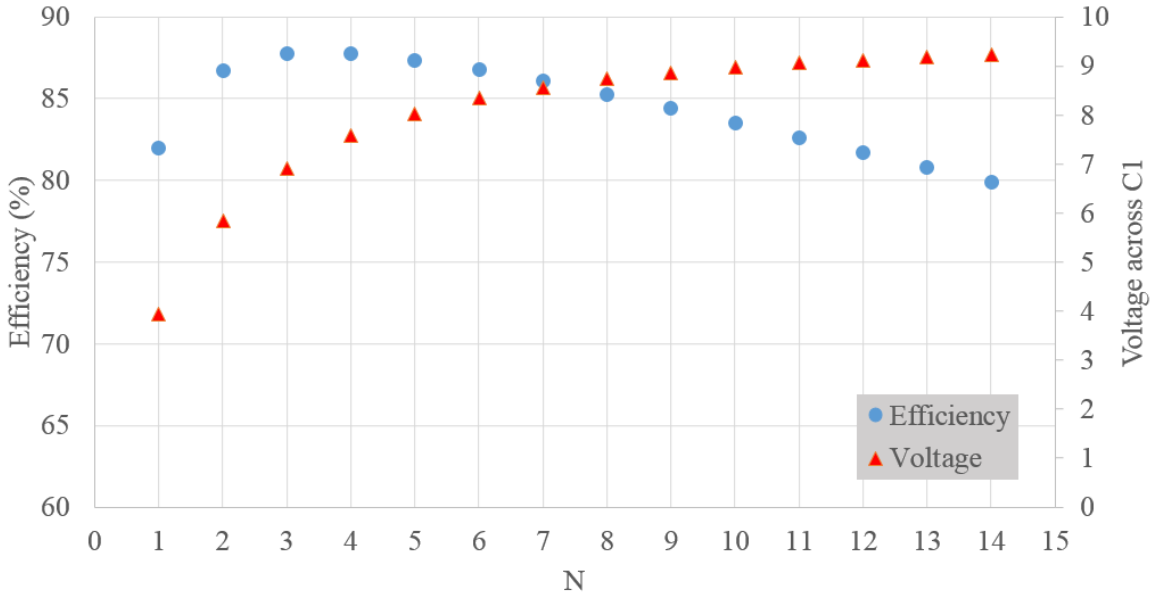

Figure 36: Simulation results for a full-wave rectifier circuit providing energy to a filter capacitor as shown above in Figure 35.

A peak efficiency level of 88% is reached after ~ 3τ, although in the range of: $(2\tau \leq t \leq 6\tau)$, the efficiency is relatively flat. Over this time-frame, the capacitor voltage is between 5.8 and 8.4V. Beyond $t = 6\tau$, the efficiency drops linearly as the capacitor node voltage saturates. Here, diodes in the full-wave rectifier continue to dissipate energy while the energy deposited into the capacitor eventually reaches zero. The saturation voltage, V_{sat} can be calculated using Eq. (26) where V_{peak} is the peak amplitude of the source and V_{fb} is the forward bias voltage of the diodes being used. The factor of two results due to the

fact that 2 diodes must conduct for each half-cycle of the input waveform in the rectification process [33].

$$V_{sat} = V_{peak} - 2V_{fb} \quad (27)$$

For these longer time-scale simulations where the capacitor is near its saturation voltage for long periods of time, the rectifier bridge continues to draw energy as the voltage source continues to charge and discharge the reverse bias capacitance of the diodes.

Rectification and DC-DC Conversion

Given the increase in power transfer efficiency for higher input voltage amplitudes to the rectifier stage, it is desirable to have higher peak voltage levels at the input of the DC-DC converter stage. For this reason, a high efficiency buck converter was selected for the DC-DC converter stage as opposed to a boost converter. For UTET applications, the input voltage can be specified through transducer design. In order for a compact circuit board footprint, a buck converter with internal switching FETs and a high frequency of operation was preferred. In general, higher frequency converters allow for smaller inductors to be used although this can lead to decreased efficiency if switching losses become dominant. The LTC3388 from Linear Technology [34] was selected as an appropriate buck converter IC as it is capable of operating with input voltages between 2.7V and 20V, and can operate with high efficiency levels (> 85 % for the expected operating range) using a small 22 µH inductor. In order to assess the efficiency of rectification and DC-DC conversion, LTspice was used to simulate the combined power transfer efficiency of a full-wave rectifier and buck-converter stage together, at 1 MHz. For

the simulation, high performance Panasonic Schottky diodes (DB2S205) were used for the full-wave rectifier using an appropriate spice model while the LTC3388 was used to simulate the DC-DC conversion. The simulation schematic is shown below in Figure 37. On the input, a 500 Ω series resistance is added to the sinusoidal source in order to simulate the high output impedance of the receive-side piezoelectric element.

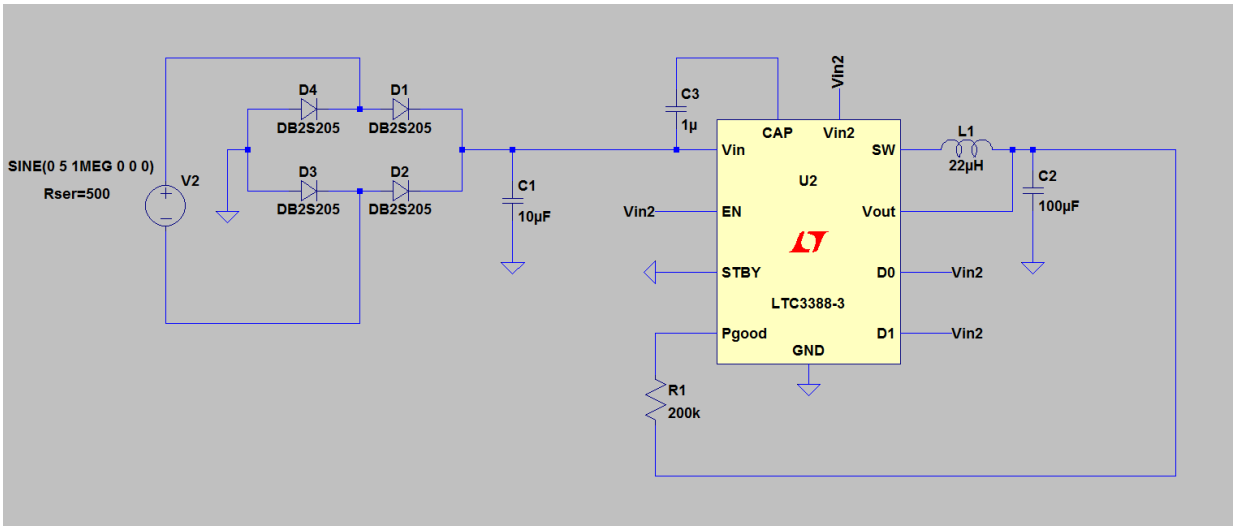

Figure 37: The simulation setup used within LTspice in order to assess the power transfer efficiency of the full-wave rectifier (Diodes D1-D4) and DC-DC converter (LTC3388-3)

The efficiency for the rectifier and DC-DC converter was inspected using four separate charging time periods, and three separate input voltage amplitudes making for a total of 12 tests. Each simulation is summarized below in Table 4.

	T1	T2	T3	T4
V1	10V, 20ms	10V, 40ms	10V, 60ms	10V, 80ms
V2	15V, 20ms	15V, 40ms	15V, 60ms	15V, 80ms
V3	20V, 20ms	20V, 40ms	20V, 60ms	20V, 80ms

Table 4: Simulation parameters for assessing PTE for the full-wave rectifier and LTC3388-3

At the end of each individual simulation, the efficiency was determine using Eq. (28).

$$\eta = \frac{E_{C1} + E_{C2}}{\int_0^T |P_{in}|} \qquad (28)$$

The calculation takes into account the total source energy provided during the course of the simulation (in its denominator). The total stored energy was found using the energy accumulated on capacitors C1 and C2 in the schematic. The results are summarized in Figure 38 below. There is an increase in efficiency for each individual simulation time (t = 20ms, t = 40ms, t = 60ms, and t = 80ms) with increases in the provided input amplitude – this is attributed to the full-wave rectifier becoming more efficient as amplitude increases. The simulations also show that different charging times have an effect on the transfer

efficiency as the capacitor approaches its steady state charge value. For the 10V amplitude simulation, the longest simulated charge cycle of 80ms is most efficient. For the 15V and 20V amplitude simulations, 60ms and 40ms simulation times generated the highest efficiencies respectively. In the completed UTET system, the transmitter will be switched off when the capacitor has reached a charged state.

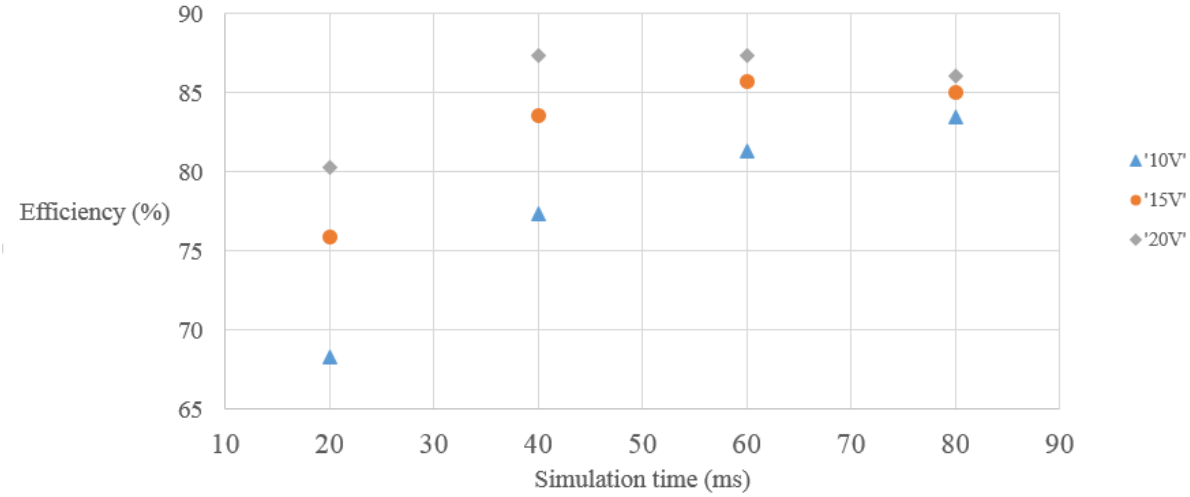

Figure 38: Power transfer efficiency versus simulation time using 3 separate input voltage amplitudes

Alternative Rectification Design Options

Given that forward voltage drop plays a significant role in the power transfer efficiency of the full-wave rectifier, an alternative circuit topology was considered for the rectification stage. Two potential solutions exist for decreasing the effects of diode forward voltage drop. One solution is to decrease the number of diodes being used in the design, while another option is to make diode forward voltage drop less relevant by increasing the provided signal amplitude. It is also possible to design a rectifier without diodes, where

actively controlled FETs replace the diodes trading VfIf losses for much smaller I^2R loss (plus the associated power for driving the FET gates and control logic). However, in this work only passive solutions were considered. A center-tapped transformer on the receive-side can be used in order to eliminate the number of required diodes and/or increase the signal amplitude. For reference, the schematic provided below in Figure 39 shows the implementation of a full-wave rectifier circuit using a center-tapped transformer and only two diodes. The positive swing of the voltage source causes diode D5 to conduct which charges C2 over a half-cycle, and during this time diode D6 blocks current from travelling through L2 on the secondary winding. On the negative half-cycle, the opposite is true and diode D6 conducts while D5 blocks current from travelling through L3 on the secondary. The design topology eliminates two diodes in the full-wave rectifier while still providing the same functionality. Additionally, the inductor windings can be sized such that they provide a voltage boost to the signal being provided.

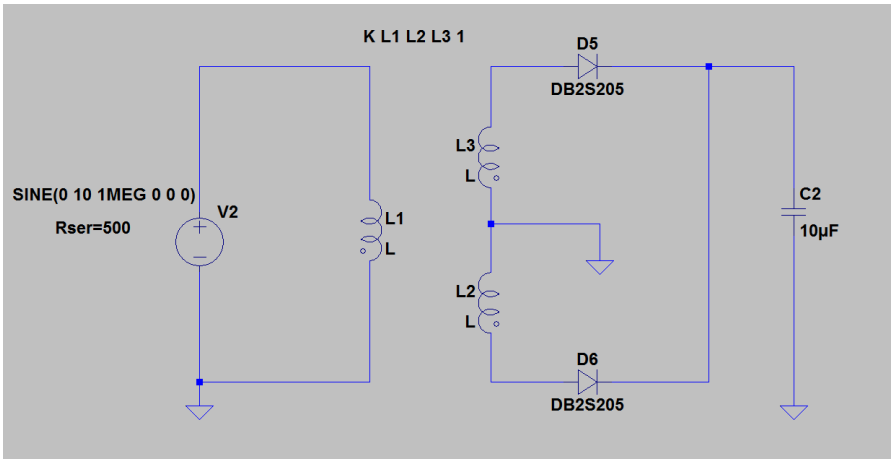

Figure 39: Full-wave rectifier schematic that makes use of a center-tapped transformer and only two diodes.

In order to assess the efficiency of this design topology and the DC-DC converter stage, the following simulation schematic was used within LTspice. For comparison purposes, a 10V amplitude simulation was run across the same simulation times as provided in Figure 38. The inductor windings were sized in a one-to-one configuration using $L2 = L3 = L4 = 1H$ purely for simulation purposes. In practice, the inductance values will be much lower (in the µH range).

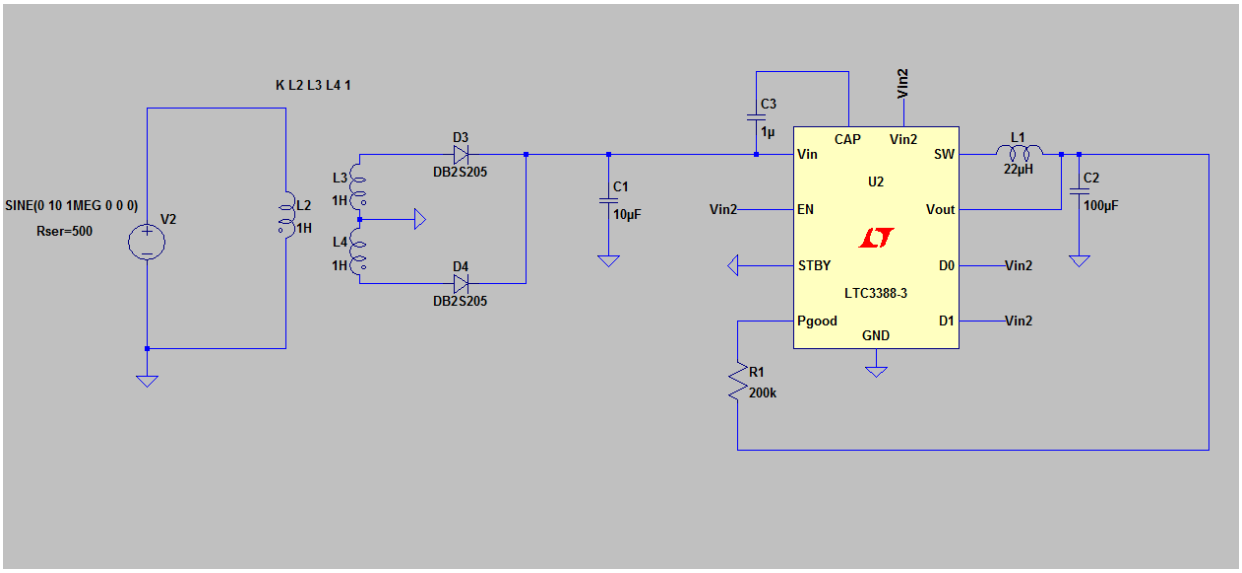

Figure 40: LTspice schematic for testing full-wave rectification and DC-DC conversion using a center-tapped transformer and 2-diodes rather than a standard full-wave rectifier using four diodes.

The simulation performance for the ideal center tapped transformer design showed an efficiency improvement of ~4.5-6.5 % over the conventional design that makes use of four diodes. However, the transformer has insertion loss associated with it which must also be considered. For reference, the formula for insertion loss is given in Eq. (29) where IL_{dB} is the insertion loss, and P_T and P_R are the transmitted and received power respectively. For

a high performance, small form-factor transformer (the ADTT1-6 surface mount RF transformer from MiniCircuits [35]), the insertion loss above 1 MHz is on the order of 0.1 to 0.2 dB resulting in losses of ~ 2 - 4.5 % which offsets the benefit of fewer diodes in the design.

$$IL_{dB} = 10 \log_{10} \frac{P_T}{P_R} \qquad (29)$$

Figure 41 shows the efficiency results comparing the full-wave rectification circuit with the center-tapped transformer (2-diode) circuit.

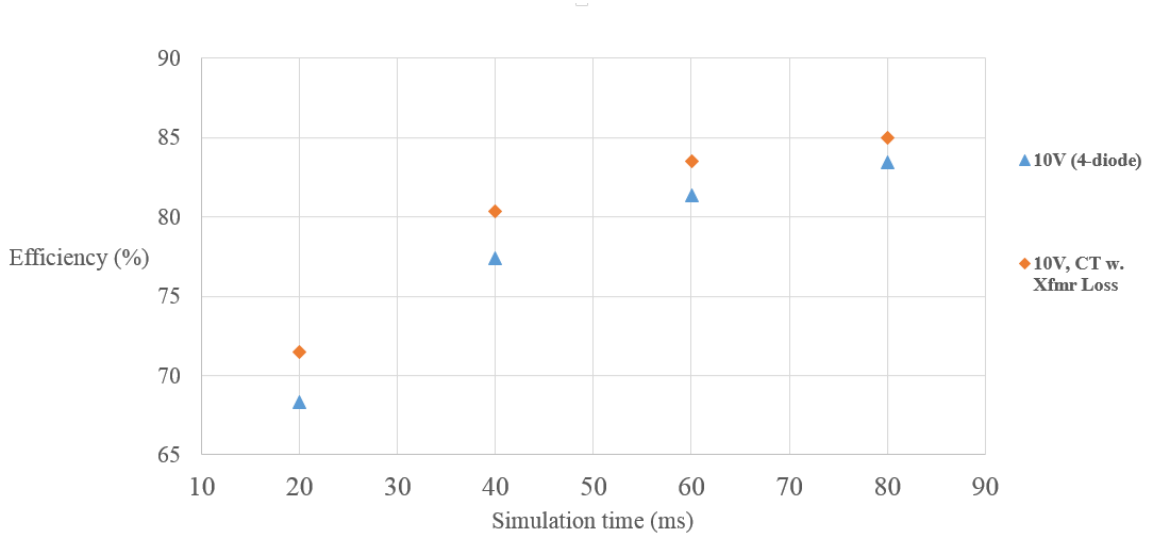

Figure 41: Efficiency results for rectification and DC-DC conversion using a conventional full-wave (4-diode) rectifier (shown with blue triangle markers), and a center-tapped transformer based rectifier using two diodes (shown with red circular markers).

Weighing the size of an implanted transformer against the slight efficiency increase, resulted in the decision to use a conventional full wave rectifier with four diodes.

Full-Wave Rectifier and LTC3388 DC-DC converter Assessment

A simplified schematic of the finalized receive-side energy harvesting circuitry is shown below in Figure 42.

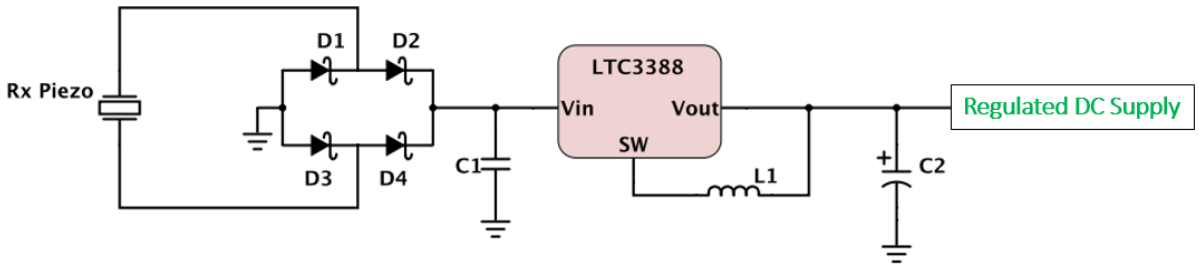

Figure 42: Receive side circuitry for energy extraction from the receiving transducer in an ultrasonic power link for AIMDs. Diodes D1-D4 make up a full-wave rectifier and C1 provides a smooth DC supply to the LTC3388., The LTC3388 is a high efficiency buck-converter that charges the energy storage element, C2, to the required DC supply (5V or 3.3V)..

The LTC3388 was first assessed on its own in order to characterize its efficiency performance. Prior to testing, a comparison was made using LTspice to investigate the steady-state performance difference between the rectifier and LTC3388-3 stage at DC and 1 MHz AC. This test showed that the steady state efficiency performance (at 1 MHz and at DC), were within 1 percentage point of each other. Thus, for simplicity, the efficiency testing was carried out using a DC input supply. The schematic for testing is shown below in Figure 43, where V1 is the DC input supply, R1 is a 150Ω resistor, and V2 is the input voltage to the LTC3388. R2 is the load resistance used to set the output power, while Vout is the regulated 3.3V output. Node voltages were measured using RMS measurements with

an Agilent oscilloscope. The input current was measured using the voltage difference between V1 and V2 and dividing by R1. The efficiency is defined as the ratio of RMS output power to RMS input power.

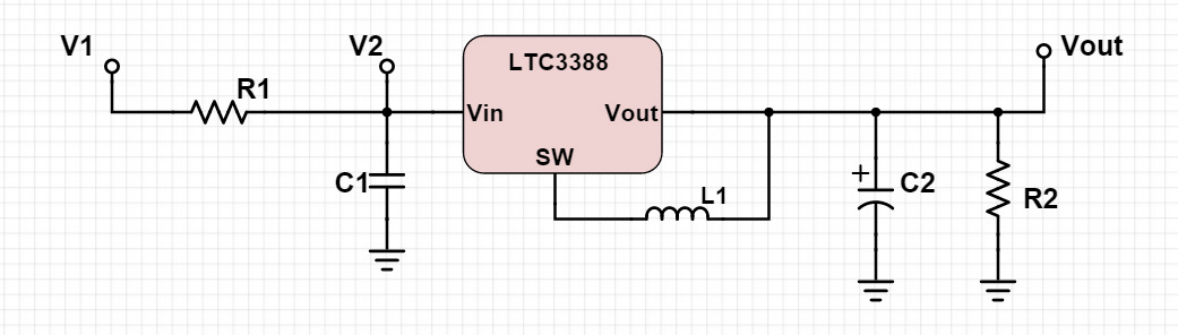

Figure 43: Test circuit for evaluating efficiency of LTC3388-3

Test measurements were performed using input voltages of ~3.3-3.6V, ~6.6V, and ~10V. A variety of output load resistances were connected across Vout in order to generate plots for efficiency versus output power. An output voltage of 3.3V was selected for this characterization. The results are summarized in Figure 44.

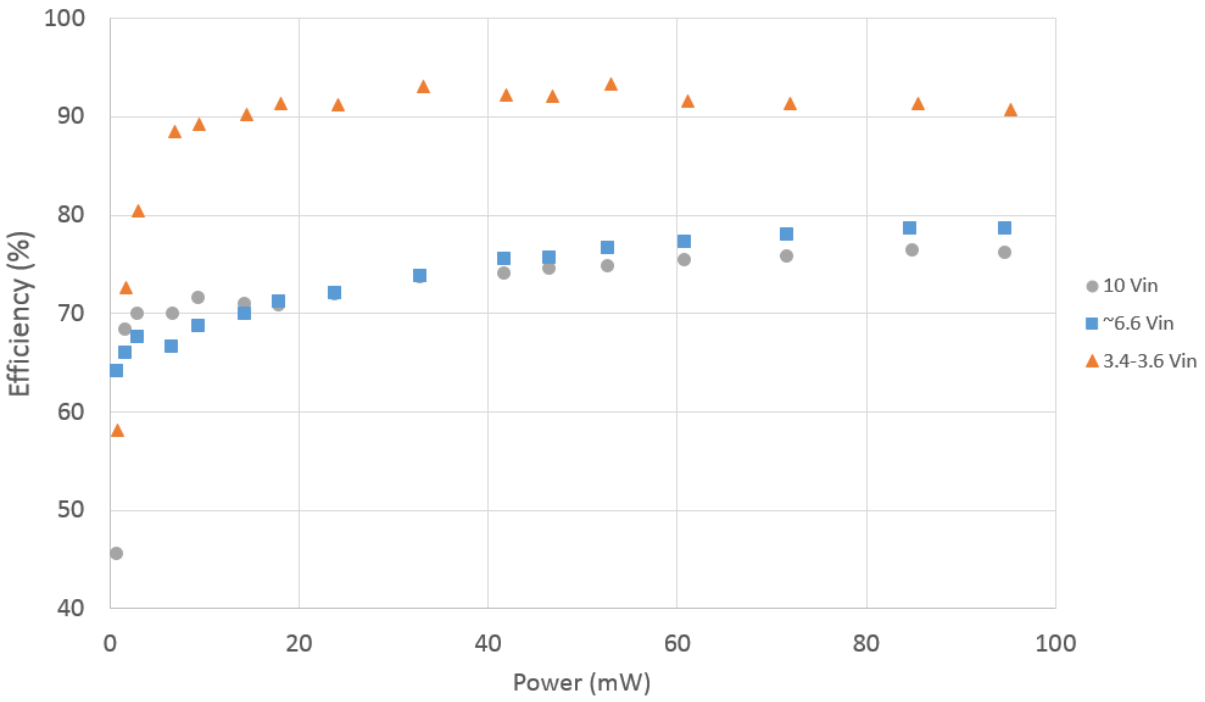

Figure 44: Efficiency vs Output Power for the LTC3388 DC-DC converter

The tests confirm that the most efficient operating point is for Vin = 3.3-3.6V, which shows a peak operating efficiency of ~ 90%. The curves for 6.6Vin and 10Vin show decreased efficiency, and saturate at approximately 80% and 76% respectively. Efficiency decreases with input voltages for the buck-converter as quiescent current losses, gate-drive losses, and transistor switch losses are all proportional to the input voltage.

Following the LTC3388 assessment, measurements were made using both the LTC3388 and a full-wave rectifier (4 Panasonic Schottky diodes – DB2S205). In this case, the measurement setup is illustrated in Figure 45 below.

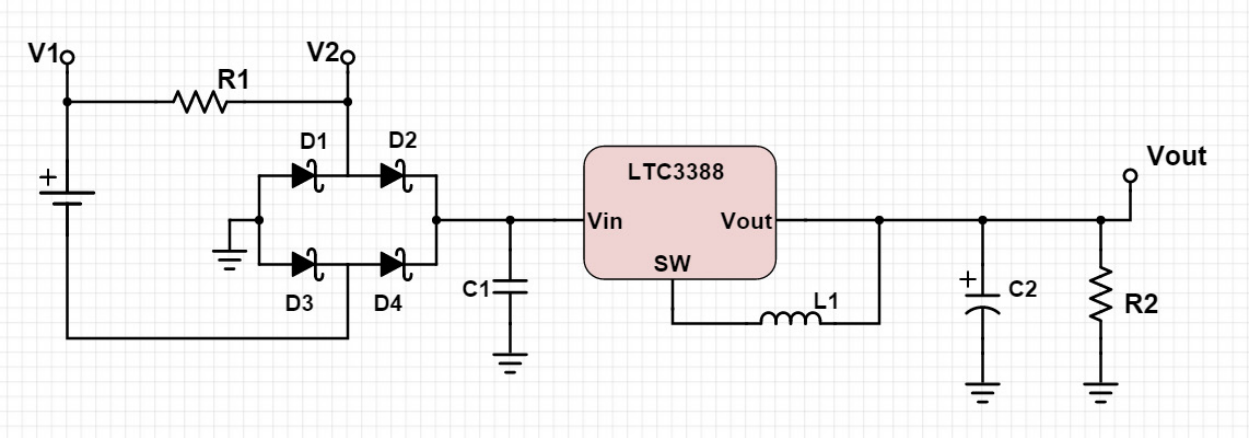

Figure 45: Full wave rectifier and LTC3388 test measurement setup

The measurement results for the full-wave rectifier and LTC3388 are summarized in Figure 46.

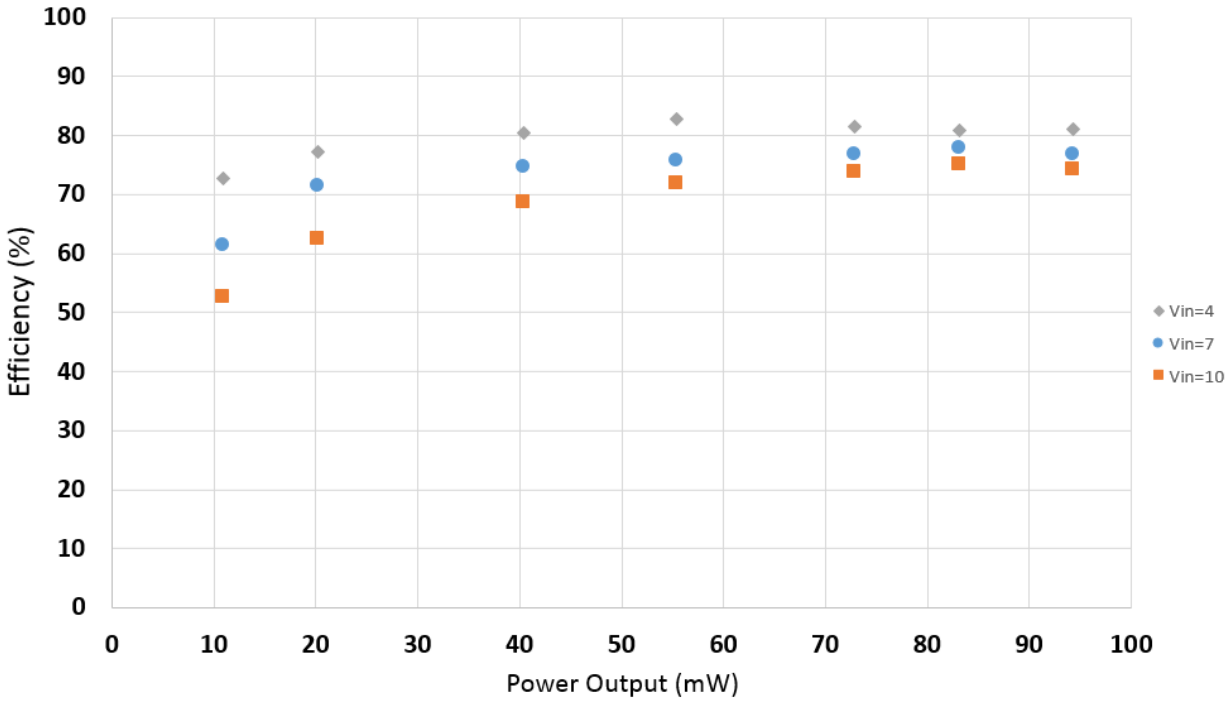

Figure 46: Efficiency vs Output Power for the LTC3388 and full-wave rectifier circuit

A peak efficiency of approximately 80% was reached using the combined LTC3388 and full-wave rectifier circuitry. Given the peak efficiency of ~90% for the LTC3388, the full-wave rectifier circuitry is estimated at ~90% for Vin = 4V and >95% for Vin = 7V and Vin=10V. As expected, the combined circuitry's efficiency saturation points are closer to one another for Vin=4V, Vin=7V, and Vin=10V due to the LTC3388 being less efficient at higher input voltages while the full-wave rectifier is more efficient with higher inputs.

Requesting Energy from the Transmitter

As explained in Chapter 3, power is to be sent from the transmitter to the receiver in an on-demand, burst-mode fashion. This burst-mode method of operation prolongs battery life in audio applications where there can be long periods of time where there is little to no sound meaning the internal electronics (acoustic driver) will be drawing little power. To implement this method of power-delivery, the ultrasonic transmitter can be controlled via feedback information from an implanted RF transceiver which will be required for audio transmission to the implanted device. A schematic illustration of the envisioned power-delivery architecture is shown below in Figure 47. On start-up, 1) the ultrasonic power-link begins sending bursts of power towards the receiver until 2) an acknowledgement is received indicating that the storage element is fully charged. Then, 3) the implanted hearing aid will draw power at a variable rate depending on external audio levels until 4) the energy storage element runs down to a level where energy is requested again via the RF transceiver.

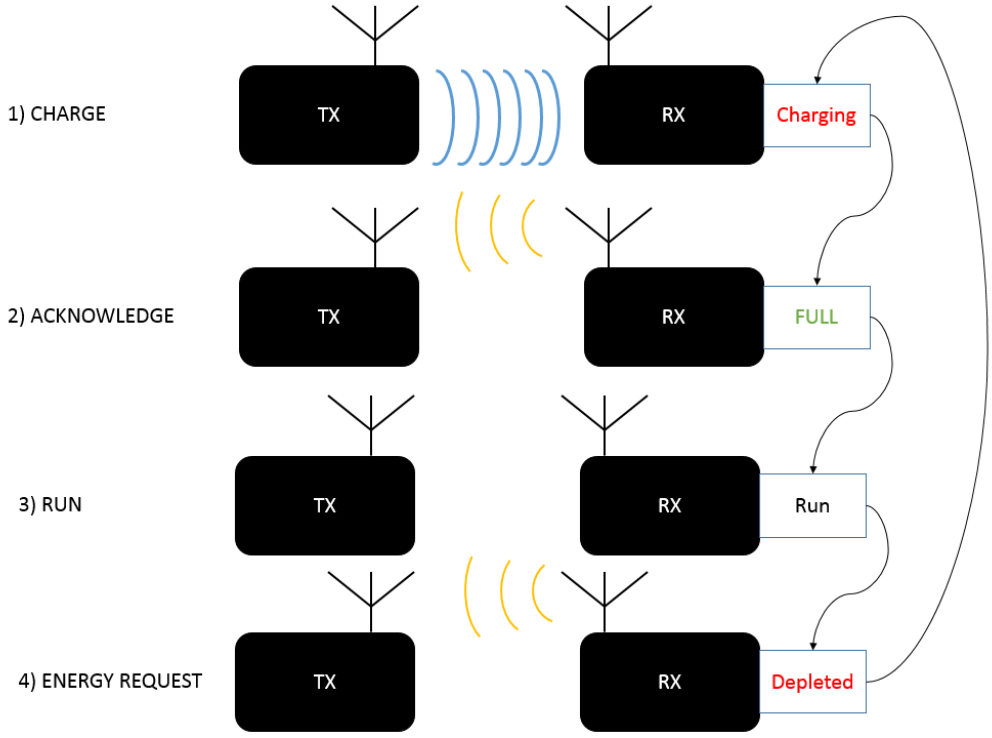

Figure 47: High-level diagram illustrating ultrasonic power delivery burst-mode architecture

The LTC3388 buck converter IC chosen for the receive-side circuitry provides an open-drain NMOS output 'Power Good' signal that can be used to facilitate the process for sending the feedback power-request signal via the RF transceiver. This Power Good signal is high-impedance when the regulated DC output is > 92% of its target value and shorted to ground otherwise. Using a pull-up resistor to a DC-supply, allows for the 'Power Good' signal to be turned into a square-wave signal that swings between Vcc and GND. This signal can be fed to an inverter in order to generate an active-high signal that becomes enabled when power is required by the receive side (i.e. the storage element voltage has fallen ~ 8% from its regulated DC value). Figure 48 shows oscilloscope traces showing the

receive-side circuit's regulated output voltage (in green), the 'Power Good' signal (in yellow), and the input capacitor voltage (in purple).

Figure 48: Receive side circuitry node-voltages. Yellow trace is 'Power Good' signal, purple trace shows input capacitor voltage, and green trace is output voltage.

Figure 49 shows two of the designed rectifier and DC-DC converter circuits, along with a Canadian quarter for size reference.

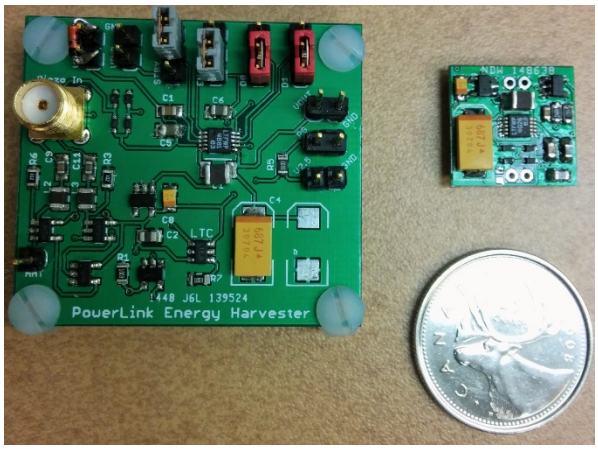

Figure 49: Rectification and DC-DC converter PCBs designed for the ultrasonic powerlink, left: original prototype for testing, right: miniaturized design

The finalized receive side circuit is characterized by a peak efficiency >80%, miniaturized size, and the ability to power 5.0V or 3.3V systems. The receive side circuit also provides a 'Power-Good' signal that can be used for regulation purposes and requesting energy from the transmit-side of the ultrasonic powerlink.

CHAPTER 5: DISCUSSION AND CONCLUSIONS

This chapter provides a summary of the main contributions that this thesis work has made to ultrasonic power transmission technologies for active implanted medical devices. Potential areas for future research efforts are also briefly discussed.

The main contributions that this thesis work has made are:

1. A thorough analysis of ultrasonic power link PTE and its sensitivity to separation distance has been presented. Following the analysis, a feedback protocol for reducing ultrasonic PTE dependence on distance was developed and shown to be effective at maintaining maximum PTE levels despite random changes in acoustic separation distance. The protocol makes use of impedance phase-measurements, and active frequency tuning in order to maintain near-constant PTE levels despite random changes in separation distance. This algorithm only requires transmit-side measurements to be made, meaning no additional implant circuitry is required making the solution attractive for miniaturized biomedical implants. Ultrasonic powerlink technology is one step closer to practical implementation after eliminating PTE dependence on separation,. A paper on this topic was published in IEEE Transactions on Biomedical Circuits and Systems: **H. Vihvelin, J. Leadbetter, M. Bance, J.A. Brown, R. Adamson, "Compensating for Tissue Changes in an Ultrasonic Power Link for Implanted Medical Devices," IEEE Transactions on Biomedical Circuits and Systems, Vol: PP, Issue: 99, 2015.** This research was also presented at the Biomedical Engineering Society (BMES) 2014 Annual Meeting in San Antonio, as an oral presentation: **H. Vihvelin, J. Leadbetter, J. Brown, R, Adamson, "Compensating**

for Tissue Changes in Ultrasonic Transcutaneous Energy Transfer Systems," Implantable Devices and Implantable Electronics Session, BMES 2014, San Antonio, Texas.

2. A discussion on amplifier classes and their suitability for high-frequency, low-power, ultrasonic powerlinks has been presented. Following the discussion, a Class E amplifier was designed for the ultrasonic powerlink, and its efficiency performance investigated in detail. A high performance gallium nitride switching transistor was shown to have improved efficiency over a traditional silicon-based devices, and we introduced for the first-time the use of eGaN FETs for high-efficiency UTET applications. A Class E amplifier was then built and characterized with a peak efficiency of 93% and efficiency levels >90% over the required frequency range. Previous amplifier designs for ultrasonic power-transmission to active implanted medical devices have been developed, but the highest reported frequency is < 700 kHz. The reported Class E amplifier in this thesis represents the most efficient known amplifier for driving ultrasonic links above 1 MHz at power levels < 400mW. A conference proceedings on the design of Class E RF amplifiers for ultrasonic links was published in the 2015 IEEE Canadian Conference on Electrical and Computer Engineering.
3. A discussion on full-wave rectification and DC-DC converter circuitry has been presented, and a receive-side circuit has been constructed and shown to provide a peak efficiency > 80%. This receiver circuit provides a regulated DC output voltage, can be used effectively on the receive-side of ultrasonic power-links, and can be implemented in a very small form factor suitable for implanted devices.

The peak system level efficiency for the ultrasonic power link and the supporting circuitry is estimated as follows:

Tx Electronics	***Ultrasonic Link***	***Rx Electronics***	***Overall Efficiency***
93%	26% (5mm Porcine Tissue)	80%	19%
93%	45% (H2O)	80%	33%

Table 5: Estimate of overall system level efficiency for the designed electronics and ultrasonic power link.

The potential areas for future research and development include:

1. The use of matching layers and how they can be used to reduce ultrasonic powerlink PTE dependence on separation distance. While frequency-tuning can be used effectively to compensate for PTE dependence on separation, a more robust solution may be to design transducers that can passively be operated at a single frequency with consistent PTE levels.
2. Improvements on the receive-side circuitry should be investigated for increasing the efficiency for the rectifier and DC-DC converter stages. While 80% efficiency is acceptable, efficiency improvements may be possible through the use of alternative circuitry such as active rectification, resonant rectification [36], and/or a more efficient DC-DC converter implementation [37].

BIBLIOGRAPHY

[1] R. R. Harrison, "Designing Efficient Inductive Power Links for Implantable Devices," in *IEEE International Symposium on Circuits and Systems, 2007. ISCAS 2007*, 2007, pp. 2080–2083.

[2] M. Soma, D. C. Galbraith, and R. L. White, "Radio-Frequency Coils in Implantable Devices: Misalignment Analysis and Design Procedure," *IEEE Trans. Biomed. Eng.*, vol. BME-34, no. 4, pp. 276–282, Apr. 1987.

[3] K. Van Schuylenbergh and R. Puers, *Inductive Powering, Basic Theory and Application to Biomedical Systems.* Springer Science, 2009.

[4] R. Bosshard, J. Muhlethaler, J. W. Kolar, and I. Stevanovic, "Optimized magnetic design for inductive power transfer coils," in *2013 Twenty-Eighth Annual IEEE Applied Power Electronics Conference and Exposition (APEC)*, 2013, pp. 1812–1819.

[5] Cochlear, "Nucleus Freedom User Manual." 2008.

[6] A. Denisov and E. Yeatman, "Ultrasonic vs. Inductive Power Delivery for Miniature Biomedical Implants," in *2010 International Conference on Body Sensor Networks (BSN)*, 2010, pp. 84–89.

[7] H. Vihvelin, J. Leadbetter, M. Bance, J. A. Brown, and R. B. A. Adamson, "Compensating for Tissue Changes in an Ultrasonic Power Link for Implanted Medical Devices," *IEEE Trans. Biomed. Circuits Syst.*, vol. PP, no. 99, pp. 1–1, 2015.

[8] J. Leadbetter, J. A. Brown, and R. B. Adamson, "The design of ultrasonic lead magnesium niobate-lead titanate (PMN-PT) composite transducers for power and signal delivery to implanted hearing aids," *Proc. Meet. Acoust.*, vol. 19, no. 1, p. 030029, Jun. 2013.

[9] S. Ozeri and D. Shmilovitz, "Ultrasonic transcutaneous energy transfer for powering implanted devices," *Ultrasonics*, vol. 50, no. 6, pp. 556–566, May 2010.

[10] S. Q. Lee, W. Youm, and G. Hwang, "Biocompatible wireless power transferring based on ultrasonic resonance devices," *Proc. Meet. Acoust.*, vol. 19, no. 1, p. 030030, Jun. 2013.

[11] H. Kawanabe, T. Katane, H. Saotome, O. Saito, and K. Kobayashi, “Power and Information Transmission to Implanted Medical Device Using Ultrasonic,” *Jpn. J. Appl. Phys.*, vol. 40, no. Part 1, No. 5B, pp. 3865–3866, May 2001.

[12] S. Suzuki, S. Kimura, T. Katane, H. Saotome, O. Saito, and K. Kobayashi, “Power and Interactive Information Transmission to Implanted Medical Device Using Ultrasonic,” *Jpn. J. Appl. Phys.*, vol. 41, no. 5S, p. 3600, May 2002.

[13] S. Arra, J. Leskinen, J. Heikkila, and J. Vanhala, “Ultrasonic Power and Data Link for Wireless Implantable Applications,” in *2nd International Symposium on Wireless Pervasive Computing, 2007. ISWPC ’07*, 2007, p. -.

[14] S. Ozeri, D. Shmilovitz, S. Singer, and C.-C. Wang, “Ultrasonic transcutaneous energy transfer using a continuous wave 650 kHz Gaussian shaded transmitter,” *Ultrasonics*, vol. 50, no. 7, pp. 666–674, Jun. 2010.

[15] Y. Shigeta, Y. Hori, K. Fujimori, K. Tsuruta, and S. Nogi, “Development of highly efficient transducer for wireless power transmission system by ultrasonic,” in *Microwave Workshop Series on Innovative Wireless Power Transmission: Technologies, Systems, and Applications (IMWS), 2011 IEEE MTT-S International*, 2011, pp. 171–174.

[16] A. Sanni, A. Vilches, and C. Toumazou, “Inductive and Ultrasonic Multi-Tier Interface for Low-Power, Deeply Implantable Medical Devices,” *IEEE Trans. Biomed. Circuits Syst.*, vol. 6, no. 4, pp. 297–308, Aug. 2012.

[17] M. O. Culjat, D. Goldenberg, P. Tewari, and R. S. Singh, “A review of tissue substitutes for ultrasound imaging,” *Ultrasound Med. Biol.*, vol. 36, no. 6, pp. 861–873, Jun. 2010.

[18] T. Lawry, “A high performance system for wireless transmission of power and data through solid metal enclosures. (Doctoral dissertation). Retrieved from ProQuest Dissertations and Theses.” Jul-2011.

[19] MEDEL, “The BONEBRIDGE Bone Conduction Implant System.” 2014.

[20] “DuraCell EasyTab 675 Zinc Air Battery.” DURACELL BATTERIES, 2006.

[21] S. H. Kim, C.-H. Yu, and K. Ishiyama, “Rotary-type electromagnetic power generator using a cardiovascular system as a power source for medical implants,” *IEEEASME Trans. Mechatron.*, vol. PP, no. 99, pp. 1–1, 2015.

[22] H. C. Government of Canada, “Guidelines for the Safe Use of Diagnostic Ultrasound,” 22-Apr-2004. [Online]. Available: http://www.hc-sc.gc.ca/ewh-semt/pubs/radiation/01hecs-secs255/index-eng.php. [Accessed: 14-Nov-2014].

[23] C. for D. and R. Health, “Guidance Documents (Medical Devices and Radiation-Emitting Products) - Guidance for Industry and FDA Staff - Information for Manufacturers Seeking Marketing Clearance of Diagnostic Ultrasound Systems and Transducers.” [Online]. Available: http://www.fda.gov/medicaldevices/deviceregulationandguidance/guidancedocuments/ucm070856.htm. [Accessed: 14-Nov-2014].

[24] H.-L. Cheng, C.-A. Cheng, C.-C. Fang, and H.-C. Yen, “Single-Switch High-Power-Factor Inverter Driving Piezoelectric Ceramic Transducer for Ultrasonic Cleaner,” *IEEE Trans. Ind. Electron.*, vol. 58, no. 7, pp. 2898–2905, Jul. 2011.

[25] Jun Honda and Jonathan Adams, “Class D amps switch on for portable applications.” 12-Jul-2005.

[26] M. K. Kazimierczuk, *RF Power Amplifiers*. John Wiley & Sons, Ltd.

[27] A. Lidow, J. Strydom, M. de Rooij, and Y. Ma, “Gallium Nitride (GaN) technology overview.” Electrical Design News (EDN), 03-Oct-2012.

[28] EPC, “EPC8002 - Enhancement Mode Power Transistor, Preliminary Specification Sheet.” 2013.

[29] F. Mazzilli, C. Lafon, and C. Dehollain, “A 10.5 cm Ultrasound Link for Deep Implanted Medical Devices,” *IEEE Trans. Biomed. Circuits Syst.*, vol. 8, no. 5, pp. 738–750, Oct. 2014.

[30] S. Davis, “Schottky Diodes: the Old Ones Are Good, the New Ones Are Better.” Power Electronics Technology, Mar-2011.

[31] “Panasonic DB2S20500L Schottky Barrier Diode.” 2010.

[32] “BAT46WJ Single Schottky barrier diode.” NXP Semiconductors, 2011.

[33] E. A. Grace, S. E. Rajan, and A. A. C. Asis, “Performance evaluation of different rectifiers for Piezo-electric energy harvesting applications,” in *2011 International Conference on Recent Advancements in Electrical, Electronics and Control Engineering (ICONRAEeCE)*, 2011, pp. 248–252.

[34] “LTC3388-1/LTC3388-3 Datasheet.” Linear Technology, 2010.

[35] "ADTT1-6 Surface Mount RF Transformer." MiniCircuits.

[36] S. Ben-Yaakov and N. Krihely, "New resonant rectifier for capacitive sources," in *2004 23rd IEEE Convention of Electrical and Electronics Engineers in Israel, 2004. Proceedings*, 2004, pp. 48–51.

[37] G. K. Ottman, H. F. Hofmann, A. C. Bhatt, and G. A. Lesieutre, "Adaptive piezoelectric energy harvesting circuit for wireless remote power supply," *IEEE Trans. Power Electron.*, vol. 17, no. 5, pp. 669–676, Sep. 2002.